

Muscle-specific Ryanodine receptor 1 properties underlie limb-girdle muscular dystrophy 2B/R2 progression

Received: 31 January 2024

Accepted: 17 March 2025

Published online: 28 March 2025



Aldo Meizoso-Huesca¹, Cedric R. Lamboley¹, James R. Krycer^{2,3},
Mark P. Hodson^{1,2,3,4}, James E. Hudson^{1,2,3} & Bradley S. Launikonis¹✉

Ryanodine receptor 1 Ca^{2+} leak is a signal in skeletal muscle, but chronic leak can underlie pathology. Here we show that in healthy male mouse, limb-girdle muscle presents higher sympathetic input, elevated ryanodine receptor 1 basal phosphorylation, Ca^{2+} leak and mitochondrial Ca^{2+} content compared to distal leg muscles. These regional differences are consistent with heat generation in resting muscle to maintain core temperature. The dysferlin-null mouse develops severe pathology in the limb-girdle but not leg muscles. Absence of dysferlin disrupts dihydropyridine receptors' inhibitory control over ryanodine receptor 1 leak, synergistically increasing leak through the already phosphorylated channel of limb-girdle muscle. This alters Ca^{2+} handling and distribution leading to reactive oxygen species production prior to disease onset. With age, oxidation of Ca^{2+} -handling proteins in dysferlin-null limb-girdle muscle alters basal Ca^{2+} movements. Our results show that muscle-specific pathology in dysferlin-null mice is linked to increased ryanodine receptor 1 Ca^{2+} leak.

Limb-Girdle Muscular Dystrophy 2B/R2 (LGMD2B/R2) is a genetic condition caused by a deficiency of the protein dysferlin that manifest as a late-onset dystrophy and selectively impact specific muscle groups as individuals age¹. Like human patients, murine models of LGMD2B show variations in muscle wasting. While muscles like the psoas and gluteus major are severely affected, others like the quadriceps, soleus, and tibialis anterior exhibit milder pathology². Yet, the underlying mechanisms responsible for these intermuscular differences remain undefined.

Dysferlin is a 230 kDa membrane protein predominantly located in the transverse (t)-tubules³, where it mediates membrane repair, structural development of the (t)-tubular system, and Ca^{2+} handling^{3–5}. Notably, dysferlin interacts with key Ca^{2+} handling players, including the dihydropyridine receptor (DHPR) and caveolin-3⁶. The DHPR interacts with the ryanodine receptor 1 (RyR1), located in the membrane of the sarcoplasmic reticulum (SR) terminal cisternae⁷ and stabilizes its resting state^{8–10}. Absence of dysferlin alters RyR1 function in

mildly dystrophic muscles following acutely applied stress¹¹. Moreover, lack of dysferlin has been proposed to alter RyR1 clustering¹².

Beyond its primary function, releasing Ca^{2+} during excitation-contraction coupling, RyR1 has multiple roles in muscle physiology, largely mediated by resting Ca^{2+} leakage into the cytosol. This leakage regulates the Ca^{2+} permeability of the t-system membrane and therefore the distribution of intracellular Ca^{2+} content¹³. Additionally, RyR1 Ca^{2+} leak participates in exercise adaptation^{14,15} and contributes to muscle thermogenesis and basal metabolism^{16–18}.

Exacerbated RyR1 leakage is associated with various myopathies, including malignant hyperthermia, central core disease, and Duchenne muscular dystrophy¹⁹. Additionally, it has been implicated in muscle wasting observed in cancer-induced cachexia and aging^{20,21}. A critical knowledge gap that remains, however, pertains to the potential role of RyR1 leak as a distinctive feature in severe versus mild progression of LGMD2B within the body.

¹School of Biomedical Sciences, The University of Queensland, Brisbane, QLD, Australia. ²QIMR Berghofer Medical Research Institute, Brisbane, QLD, Australia. ³School of Biomedical Sciences, Queensland University of Technology, Brisbane, QLD, Australia. ⁴School of Pharmacy, The University of Queensland, Brisbane, QLD, Australia. ✉ e-mail: b.launikonis@uq.edu.au

Here, we explored the link between RyR1 function and the prognosis of LGMD2B/R2. For this, we compared Ca^{2+} handling properties and proteomic profiles of murine muscles known to exhibit varying degrees of pathology. We compared the severely affected psoas muscle against two mildly affected muscles, the tibialis anterior (TA) and extensor digitorum longus (EDL). Here we show intrinsic differences in RyR1 function and Ca^{2+} handling between wild-type psoas and TA/EDL. These distinctions were characterized by greater RyR1 Ca^{2+} leak, increased basal RyR1 phosphorylation, and a differential distribution of fibre Ca^{2+} , with higher mitochondrial Ca^{2+} content in WT psoas. These differences trace back to higher nor-epinephrine concentration in psoas relative to TA, accompanied by increased PKA signalling. In absence of dysferlin, these Ca^{2+} handling disparities were further exacerbated in psoas but not in TA prior to the dystrophic phenotype and progressed over time. Furthermore, proteomic analysis identified enrichment of thermoregulation and metabolic adaptation to RyR1 leak in WT psoas that was not observed in WT TA. These findings highlight a potential divergence in the

thermogenic capacity between core and distal muscles in mice, potentially aimed at optimizing heat generation in proximity to internal organs. In the murine psoas, RyR1 channels operate in a chronically leaky state; however, lack of dysferlin exacerbates RyR1 leakage, contributing to the localized progression of the disease observed in this muscle.

Results

Inherent difference in RyR1 Ca^{2+} leak between healthy muscles is exacerbated in the absence of dysferlin

The selection of the psoas as a representative muscle of severe dystrophic presentation and the TA and EDL as representative muscles of mild dystrophic presentation in the BlaJ mouse was based on previous observations^{2,22} and confirmed by H&E staining and muscle weights at 8 and 36 weeks old (Fig. 1a–c; Sup Fig. 1a–d). In the main body of this article, we will concentrate on using the TA as the example of a mildly dystrophic muscle in dysferlinopathy. Supporting data on mildly dystrophic EDL muscle is provided in the supplement.

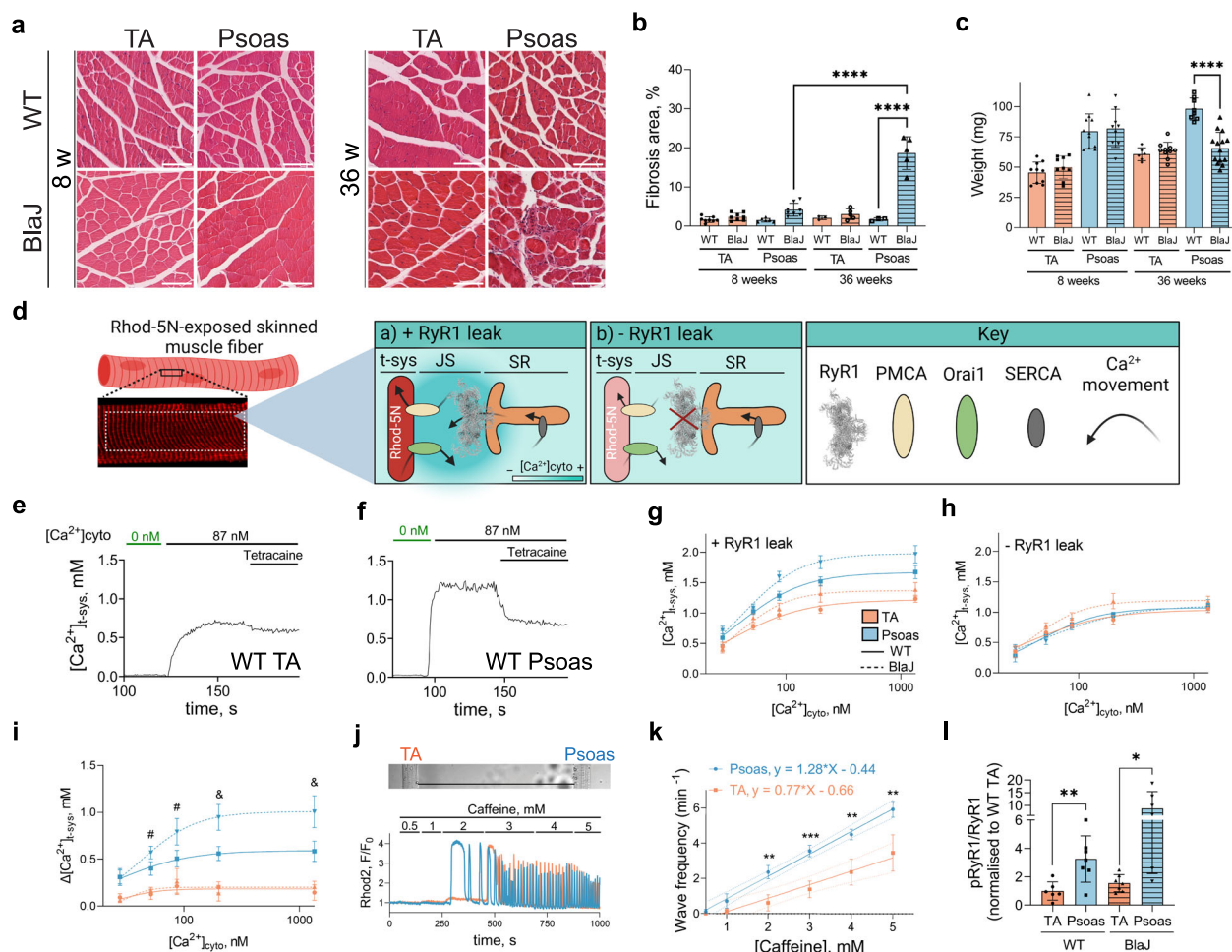


Fig. 1 | Dysferlin deficiency exacerbates intrinsic differences in RyR1 leak between Psoas and TA prior to the development of dystrophic phenotype.

a H&E staining of WT and BlaJ muscles (8 and 36 weeks-old mice). **b** Fibrosis area calculated as percentage of total cross-sectional muscle area. $n = 3-8$. **c** Muscle weights from WT and BlaJ mice. $n = 6-14$. **d** Diagram showing t-system-trapped rhod-5N to measure RyR1 Ca^{2+} leak. RyR1 Ca^{2+} leak sets the $[\text{Ca}^{2+}]_{\text{t-sys}}$ above the bulk cytosol. $[\text{Ca}^{2+}]_{\text{t-sys}}$ directly influences PMCA activity and $[\text{Ca}^{2+}]_{\text{t-sys}}$. When RyR1 leak is inhibited, $[\text{Ca}^{2+}]_{\text{t-sys}}$ drops proportional to the drop in $[\text{Ca}^{2+}]_{\text{cyto}}$. **e, f** Representative $[\text{Ca}^{2+}]_{\text{t-sys}}$ (t) during exposure to 1 mM Tetracaine in a WT TA (**e**) and WT psoas (**f**) fibre. **g** Steady-state $[\text{Ca}^{2+}]_{\text{t-sys}}$ across a range of $[\text{Ca}^{2+}]_{\text{cyto}}$ in presence (**g**) and absence (**h**) of RyR1 leak. $n = 5-17$ fibres. **i** RyR1 Ca^{2+} leak by means of $\Delta[\text{Ca}^{2+}]_{\text{t-sys}}$

($[\text{Ca}^{2+}]_{\text{t-sys}}$ before – after 1 mM tetracaine). $n = 5-13$ fibres. **j** (Top) Bright field image of two fibres (TA and psoas, both WT) aligned for simultaneous imaging. Scale bar: 400 μm . (Bottom) Spatially averaged Rhod-2 (cytosolic) profiles from a TA (orange) and a psoas (blue) fibre upon exposure to increasing [Caffeine]. **k** Ca^{2+} wave frequency across a range of [Caffeine]. $n = 7$ preparations. **l** RyR1 phosphorylation (Ser2844) relative to non-phosphorylated RyR1. Data normalized to WT TA. Data are presented as mean \pm SD (**b, c, l**) or \pm SEM (**g, h, i, k**). **e–l** 8 weeks-old groups. Statistical analysis: (**b, c, l**), one-way ANOVA with Tukey's multiple comparison. **i** two-way ANOVA. (#) Two significant results; (&) Five significant results. (**k**), paired T-test. (**l**), unpaired (multiple) t-tests. **** $p < 0.0001$, ** $p < 0.01$, * $p < 0.05$. Source data are provided as a Source Data file.

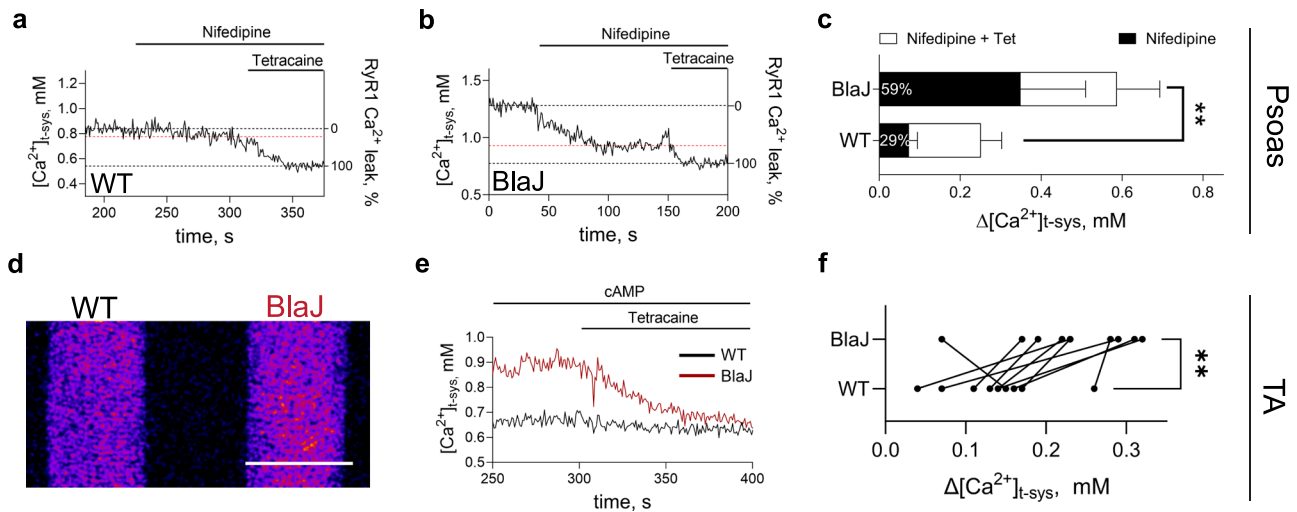


Fig. 2 | Lack of dysferlin synergistically increases RyR1 leak via DHPR destabilization and RyR1 phosphorylation. **a, b** Representative $[Ca^{2+}]_{t-sys}(t)$ in WT (**a**) and BlaJ (**b**) psoas fibre during sequential perfusion of nifedipine (5 mM) and tetracaine (1 mM). **c** Percentage of nifedipine-sensitive (black) and nifedipine-insensitive RyR1 leak WT and BlaJ psoas fibres. $n = 5-8$. **d** T-system rhod-5N confocal image of two TA fibres placed in parallel to each other for simultaneous live imaging. Scale bar:

100 μm . **e** Representative simultaneous $[Ca^{2+}]_{t-sys}$ traces from WT and BlaJ TA fibres exposed to cAMP (100 mM) and tetracaine (1 mM) subsequently. **f** Tetracaine-induced $\Delta[Ca^{2+}]_{t-sys}$ of cAMP-exposed WT and BlaJ TA fibres. Summary of results shown in (**e**). $n = 7$. **a-f** 8 weeks-old fibres. Statistical analysis in (**c**), unpaired t-test. Statistical analysis in (**f**), paired t-test. $**p < 0.01$. Source data are provided as a Source Data file.

First, RyR1 leakiness was measured in 8 weeks-old psoas and TA fibres leveraging the high sensitivity of the t-system Ca^{2+} concentration ($[Ca^{2+}]_{t-sys}$) to RyR1 Ca^{2+} leak in resting skinned muscle fibres (see Methods). Noteworthy, this age was chosen to minimise potential confounding effect of the dystrophy that presents disproportionately across muscles later in BlaJ mice.

Due to its large surface-to-volume ratio and low endogenous Ca^{2+} buffers, the $[Ca^{2+}]_{t-sys}$ responds to $[Ca^{2+}]_{cyto}$ at the junctional space ($[Ca^{2+}]_j$), set by the extent of RyR1 Ca^{2+} leak. This sets PMCA activity, pumping Ca^{2+} into the t-system lumen in a $[Ca^{2+}]_j$ -dependent fashion^{23,24}. Thus, the leak of Ca^{2+} from the RyR1 rapidly changing the $[Ca^{2+}]_j$ is detected by t-system-trapped rhod-5N^{13,23}. RyR1 Ca^{2+} leak is quantified by comparing $[Ca^{2+}]_{t-sys}$ in the absence and presence of saturating concentrations of the RyR1 antagonist tetracaine²⁵ (Fig. 1d). Figure 1e, f show $[Ca^{2+}]_{t-sys}$ profiles over time ($[Ca^{2+}]_{t-sys}(t)$) from 8 weeks-old WT TA and WT psoas fibres, respectively. Tetracaine-induced RyR1 inhibition exerted a slight decrease in $[Ca^{2+}]_{t-sys}$ in TA (Fig. 1e), whereas a substantial depression of $[Ca^{2+}]_{t-sys}(t)$ was observed in psoas (Fig. 1f). This assay was performed in both WT and BlaJ TA and psoas fibres across a range of $[Ca^{2+}]_{cyto}$ (28–1342 nM), as RyR1 leakiness is expected to increase as the SR loads upon higher $[Ca^{2+}]_{cyto}$. Figure 1g, h show the resting $[Ca^{2+}]_{t-sys}$ as a function of $[Ca^{2+}]_{cyto}$ for each group in absence and presence of tetracaine, respectively.

The extent of RyR1 Ca^{2+} leak ($\Delta[Ca^{2+}]_{t-sys}$) was plotted against the experimental $[Ca^{2+}]_{cyto}$ (Fig. 1i), showing that WT psoas presents greater RyR1 leak compared to WT TA ($p < 0.05$ at 200 nM $[Ca^{2+}]_{cyto}$; $p < 0.01$ at 1342 nM $[Ca^{2+}]_{cyto}$). Furthermore, BlaJ psoas displayed higher RyR1 leak compared to WT psoas ($p < 0.05$ at 200 nM $[Ca^{2+}]_{cyto}$; $p < 0.01$ at 1342 nM $[Ca^{2+}]_{cyto}$). No differences were observed between the TA groups (WT vs BlaJ). Results obtained from EDL fibres (WT and BlaJ) resembled those from TA, consistent with the mild development of pathology in TA and EDL of BlaJ mice (Supplementary Figure 1a–f).

To confirm the differences in RyR1 function between WT psoas and TA fibres in an assay that would not rely on the fibre t-system, we tested fibres response to increasing [caffeine] to generate repetitive Ca^{2+} waves²⁶. Ca^{2+} transients from a skinned TA fibre and a skinned psoas fibre from the same WT mouse were simultaneously monitored during exposure to progressively increasing [caffeine] (Fig. 1j &

Supplementary movie 1). Psoas exhibited higher caffeine sensitivity and showcased greater wave frequency compared to TA (2 mM, $p < 0.005$; 3 mM, $p < 0.0005$; 4 mM, $p < 0.01$; 5 mM, $p < 0.01$), providing additional evidence of a less stable RyR1 in WT psoas relative to TA (Fig. 1j, k).

Since RyR1 phosphorylation is linked to increased RyR1 Ca^{2+} leak^{20,26}, we tested whether this feature differed between the two WT groups, potentially explaining the differences in RyR1 leakage between WT TA and psoas. For this, we examined phosphorylation of the RyR1 via targeted mass spectrometry. This revealed a 3-fold increase in basal RyR1 phosphorylation in psoas relative to TA at Ser2844. Notably, comparable trends were observed across BlaJ muscles (Fig. 1l, Supplementary Table 4). Together, the results in Fig. 1 show that between the WT muscles, psoas exhibits higher RyR1 leak than TA, associated with a greater channel phosphorylation in psoas. Moreover, in the absence of dysferlin, RyR1 leak is exacerbated in psoas prior to the severe dystrophic phenotype but not in TA, where the pathology is milder throughout the lifespan of the mouse.

Next, we explored the mechanisms contributing to (1) the increased RyR1 leak in BlaJ psoas and (2) the muscle-specific nature of this increase, observed only in psoas. Previous studies have shown that DHPR modulators restore RyR1 function in dysferlin-null fibres¹¹. Therefore, we assessed whether this was the case for 8 weeks-old WT and BlaJ psoas fibres (Fig. 2a, b). Notably, nifedipine blunted 59.5% of the RyR1 leak in BlaJ fibres but only accounted for 29.3% of the RyR1 leak in WT (Fig. 2c, $p < 0.01$). To validate that nifedipine decreased $[Ca^{2+}]_{t-sys}$ by modulating RyR1 leak (via the DHPR) and not blocking any potential Ca^{2+} leak through the DHPR, we exposed fibres to tetracaine, maximally blocking RyR1 leak, before perfusing nifedipine. Under these conditions, nifedipine had no impact on $[Ca^{2+}]_{t-sys}$, confirming that its former effect was solely due to an indirect modulation of RyR1 leak (Supplementary Figure 2).

As a further control, we directly targeted RyR1 leak by increasing $[Mg^{2+}]_{free}$ from 1 to 3 mM²⁷. This approach allowed evaluation of RyR1 leak inhibition bypassing the DHPR-RyR1 interaction. Mg^{2+} -induced RyR1 inhibition was comparable between both genotypes (Supplementary Figure 3), indicating that the functional disparities in RyR1 leak between genotypes stem from the DHPR-RyR1 interaction as opposed to intrinsic properties of the RyR1 channels.

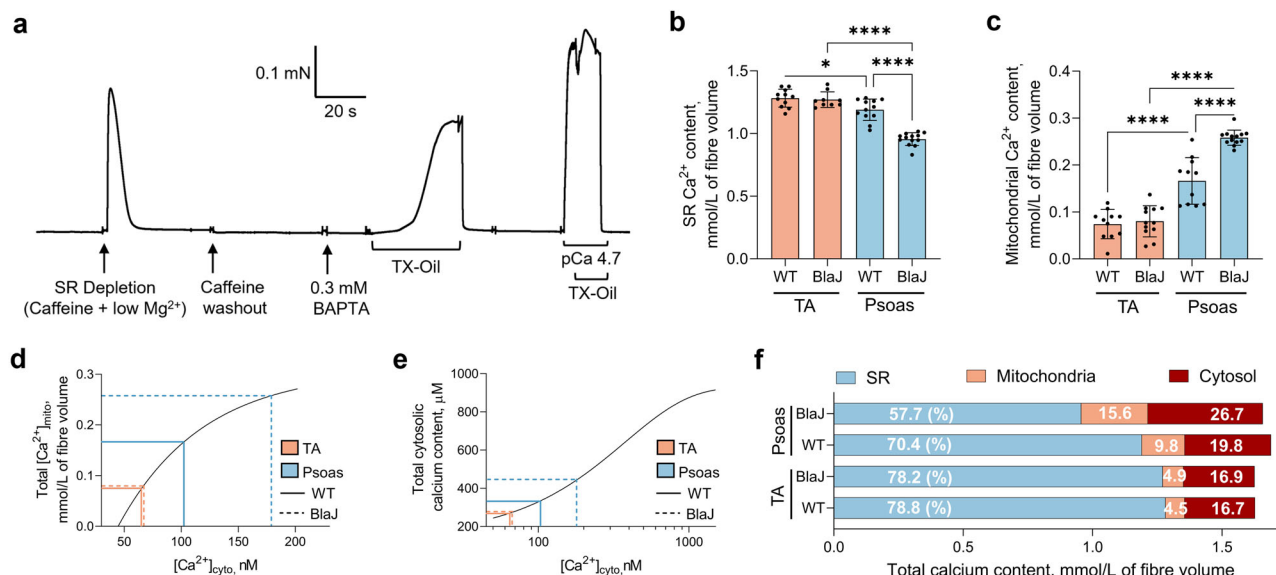


Fig. 3 | Differences in intracellular Ca^{2+} distribution across WT TA and psoas increase in absence of dysferlin. a Representative BAPTA-lysis experimental trace. A mechanically skinned mouse psoas fibre segment with endogenous resting Ca^{2+} content was depleted of SR calcium and then equilibrated with known free [BAPTA]. TX-Oil-induced lysis produces ~45% of the maximal force. Force response (relative to maximal response) in conjunction with pCa and known [BAPTA] employed, enables quantification of total Ca^{2+} released upon lysis. **b, c** Endogenous Ca^{2+} content (SR, **b**; mitochondrial, **c**) in TA and psoas fibres from WT and BlaJ

muscles. $n = 9-13$. Data presented as Mean \pm SD. **d** Estimation of resting $[Ca^{2+}]_{cyto}$ across TA and psoas (WT and BlaJ) derived from total mitochondrial Ca^{2+} . **e** Estimation of total cytosolic Ca^{2+} bound to cytosolic Ca^{2+} buffers. Mathematical model obtained from Lamboley et al.¹³. **f** Ca^{2+} content (per fibre volume) of the major subcellular calcium compartments in TA and psoas (WT and BlaJ), shown as cumulative histograms. **a-f** 8 weeks-old. Statistical analysis in **b** and **c** were performed with one-way ANOVA with Tukey's multiple comparison. **** $p < 0.0001$, * $p < 0.05$. Source data are provided as a Source Data file.

As the impact of the absence of dysferlin on the DHPR is expected to manifest across all muscles, we hypothesized that the increase of RyR1 leak observed specifically in BlaJ psoas might arise from a synergistic interplay between mechanisms destabilizing the RyR1. Given that WT psoas exhibits a higher basal RyR1 phosphorylation compared to TA, we postulated that this baseline disparity could heighten RyR1 sensitivity to DHPR dysregulation in the absence of dysferlin. To investigate this, we simultaneously exposed WT and BlaJ TA fibres positioned in parallel in the same experimental chamber to cAMP (Fig. 2d), a known inducer of RyR1 phosphorylation at Ser2844^{26,28,29}. In this experimental approach, the two skinned fibres shared the same cytoplasmic environment. Subsequently, cAMP-pre-exposed fibres were subjected to tetracaine to assess their RyR1 leak. Interestingly, cAMP increased RyR1 leak more in BlaJ TA compared to WT, consistent with a compounding effect of RyR1 phosphorylation and DHPR dysregulation on RyR1 leak (Fig. 2d-f).

RyR1 Ca^{2+} leak coordinates fibre Ca^{2+} distribution independently of dysferlin

Increases in RyR1 leakage trigger intracellular Ca^{2+} content redistribution within the muscle, thereby influencing its function¹³. Given the differences in RyR1 Ca^{2+} leak between WT psoas and TA, and the exacerbation of RyR1 leak in BlaJ psoas, we assessed the fibre Ca^{2+} content and distribution across the SR and mitochondria of the four 8 weeks-old groups. For this, we utilized a membrane lysis method, enabling us to quantify compartmentalised Ca^{2+} content with high resolution based on fibre force response upon intracellular membrane lysis at a known [BAPTA]^{30,31} (Fig. 3a) (see Methods).

In line with its greater RyR1 leak, WT psoas presented a lower SR Ca^{2+} content than WT TA (Fig. 3b) (1.19 ± 0.08 mmol/L vs 1.28 ± 0.07 mmol/L, $p < 0.05$). Additionally, reduced SR Ca^{2+} content in BlaJ compared to WT was observed only in psoas (0.95 ± 0.05 vs 1.19 ± 0.08 mmol/L, $p < 0.0001$) (Fig. 3b). Inversely to these patterns, psoas displayed a higher mitochondrial Ca^{2+} content than TA in WT mice (0.166 ± 0.05 vs 0.074 ± 0.03 mmol/L, $p < 0.0001$) (Fig. 3c).

Furthermore, BlaJ psoas exhibited greater mitochondrial Ca^{2+} content compared to WT psoas (0.258 ± 0.02 vs 0.166 ± 0.05 mmol/L, $p < 0.0001$). The mitochondrial Ca^{2+} content values obtained were integrated into a previously established model to estimate the cytoplasmic Ca^{2+} content across the different groups^{13,32} (Fig. 3d, e). Notably, the sum of SR, mitochondria and cytosolic Ca^{2+} revealed that despite the changes in intracellular Ca^{2+} distribution across the groups, the total calcium content is preserved (Fig. 3f). Overall, Fig. 3 shows that the intracellular Ca^{2+} content distribution varies between WT psoas and TA and that Ca^{2+} content redistribution occurs in the absence of dysferlin in psoas, where RyR1 Ca^{2+} leak increases.

Thermogenic specialization of mouse psoas

The greater RyR1 basal phosphorylation and Ca^{2+} leak in WT psoas compared to TA and EDL, along with its higher mitochondrial Ca^{2+} content, suggest differential basal signalling within the muscles. Since Ser2844 of the RyR1 is a PKA-dependent phosphorylation site, we assessed whether PKA signalling was different between TA and psoas. Compared to TA, psoas presented higher phosphorylated PKA substrates, indicating that overall PKA basal signalling is constitutively elevated in psoas (Fig. 4a, b). Consistent with the increased basal PKA signalling and RyR1 phosphorylation (Fig. 1l), psoas displayed higher norepinephrine concentration compared to TA (Fig. 4c).

The differences in Ca^{2+} handling, traced back to higher basal sympathetic input in psoas, suggest a functional difference between these muscles. To explore the physiological significance underlying these differences, we compared the proteomic profiles of WT TA and psoas. Interestingly, analysis of KEGG pathways represented by psoas and TA-specific proteins revealed enrichment in thermogenesis in psoas that was not present in TA (Fig. 4d), represented by proteins such as UCP1, fatty acid metabolism-related proteins, members of the Ras GTPase family and electron transport chain-related proteins (Supplementary Table 5). Gene Ontology (GO) enrichment analysis from SWATH data revealed important differences across the significantly enriched biological processes represented by the most

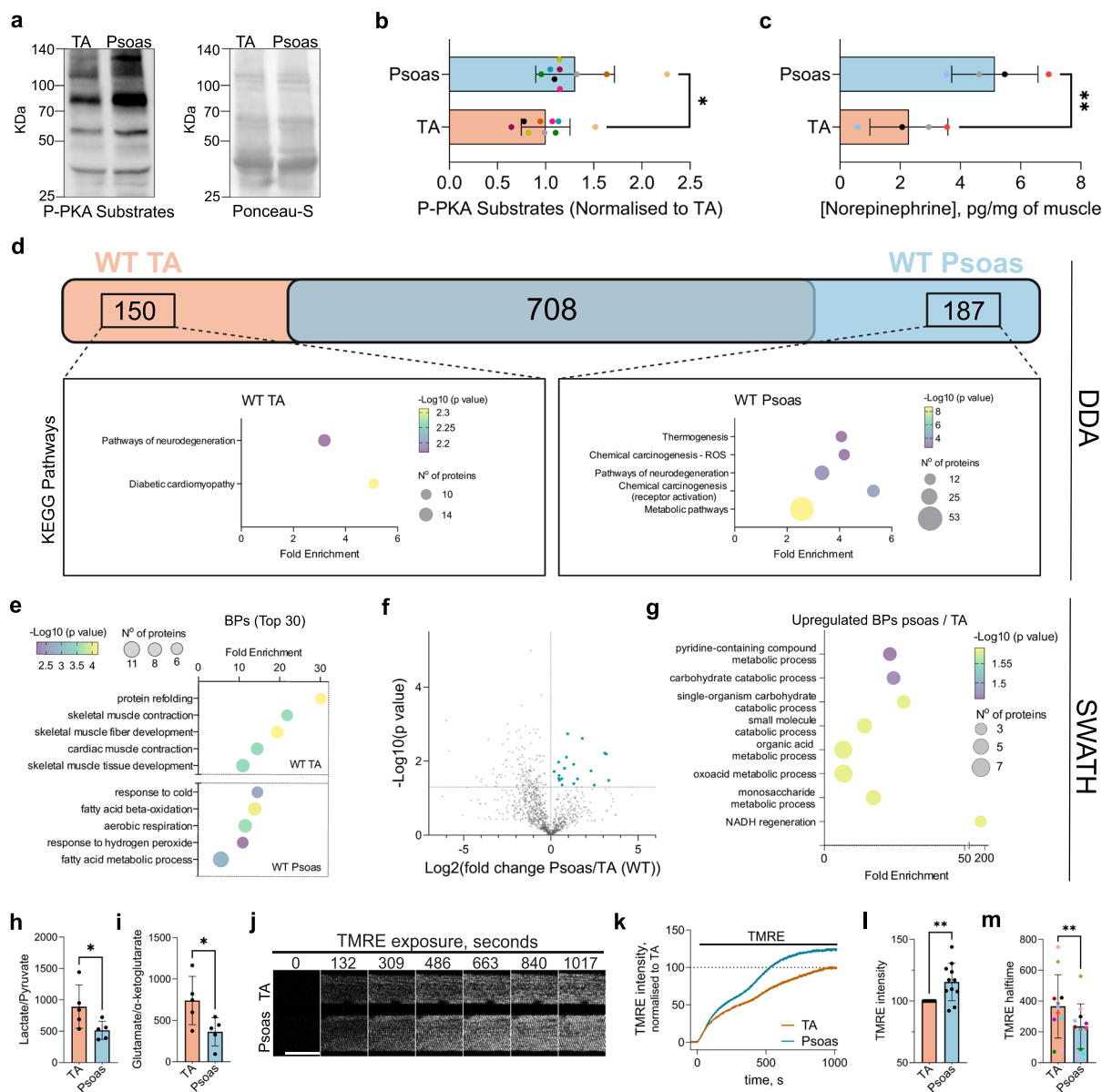


Fig. 4 | Psoas exhibits a distinctive thermogenic program compared to TA.

a Western blot against p-PKA substrates (left) and Ponceau-S signal (right) in TA and Psoas muscle homogenates (8 w/o, WT). **b** Densitometry of anti p-PKA substrate antibody signal normalised to Ponceau-S signal. $n = 9$. **c** Quantification of norepinephrine concentration in TA and Psoas (8 weeks old, WT) $n = 4$. **d** (Top) Venn diagram showing identified proteins in WT Psoas and WT TA by Data-Dependent Acquisition (DDA) workflow. (Bottom) Kegg pathways represented by the WT Psoas and WT TA-specific proteins identified through DDA workflow. Terms were filtered by the criteria of ≥ 10 proteins and adjusted p -value (Benjamini) < 0.05 . **e** TA and Psoas-exclusive biological processes revealed by Gene Ontology (GO) enrichment analysis of 180 most abundant proteins in WT TA (top) and WT Psoas (bottom) (8 weeks old) revealed by SWATH workflow. Terms were filtered by the criteria of ≥ 6 proteins and adjusted p -value (Benjamini) < 0.05 . **f** Volcano plot of total quantified

proteins showing significantly increased (blue) protein content in WT Psoas relative to WT TA. **g** GO biological process analysis of upregulated proteins in WT Psoas relative to WT TA. Terms filtered by adjusted p -value (Benjamini) < 0.05 .

h, i Metabolites ratio (Lactate/Pyruvate, **h** Glutamate/a-ketoglutarate, **i** present in WT TA and Psoas (8 weeks old). $n = 5$. **j** Simultaneous confocal imaging of 150 nM Tetramethylrhodamine, Ethyl Ester (TMRE) uptake in a WT TA and a Psoas fibre. Scale bar = 50 μm . **k** TMRE fluorescence profile over time in TA (orange) and Psoas fibre (blue) (derived from **j**). **l** TMRE intensity after plateau in TA and Psoas fibres (normalised to TA). **m** TMRE halftime in TA and Psoas fibres (normalised to TA). $n = 11$. Statistical analysis in (**b, c, l, m**) were performed with paired T-test. $**p < 0.01$, $*p < 0.05$. Statistical analysis in **h&i** were performed with an unpaired one-tailed T-test. Source data are provided as a Source Data file.

abundant proteins in each muscle (Supplementary Figure 4; Supplementary Tables 6, 7). While TA displayed enriched processes mainly associated with contraction, Psoas exhibited terms associated with thermogenesis and metabolism, such as *response to cold*, *response to hydrogen peroxide*, and *fatty acid metabolism* (Fig. 4e). This finding is in line with the greater norepinephrine concentration and RyR1 Ca^{2+} leak observed in Psoas, as this feature constitutes a thermogenic source in mammalian skeletal muscle^{17,26}. Furthermore, this is expected to enhance metabolism to meet the increased energy

demands associated with thermogenesis, as suggested by the proteomic analysis.

Furthermore, GO enrichment analysis of biological processes of the significantly upregulated proteins in Psoas vs TA revealed *NADH regeneration* as the biological process with the highest fold enrichment (Fig. 4f, g; Supplementary Table 8). This observation aligns with the distinctive feature of the Psoas showing elevated RyR1 Ca^{2+} leak compared to TA, which sets the resting ATP resynthesis rate¹⁷ and enhances NADH-dependent mitochondrial respiratory capacity³³. In line with

this, metabolomic analysis revealed that WT psoas displays a lower NADH/NAD⁺ ratio in both cytosol and mitochondrial cisternae, relative to WT TA, as revealed by a lower ratio of lactate:pyruvate ($p < 0.05$) and glutamate:α-ketoglutarate ($p < 0.05$)^{34,35}, respectively (Fig. 4h, i). Therefore, upregulation of NADH regeneration in psoas likely represents a compensatory mechanism to meet the increased demand for NADH. Furthermore, psoas fibres presented elevated mitochondrial membrane potential compared to TA, indicated by increased TMRE uptake (Fig. 4j–m) ($p < 0.01$). Collectively, Fig. 4 shows that psoas presents an increased thermogenic capacity compared to TA, as well as higher sympathetic input in basal conditions; this is consistent, and likely supports, the increased RyR1 phosphorylation and Ca²⁺ leak, as well as the raised mitochondrial Ca²⁺ in psoas compared to TA and EDL in WT mouse.

Elevated RyR1 Ca²⁺ leak leads to t-system Ca²⁺ handling protein oxidation and functional impairment

The raised mitochondrial Ca²⁺ content in psoas (Fig. 3) is expected to promote the generation of reactive oxygen species (ROS). Accordingly, Blaj mice have been found to display oxidative stress, attenuated by N-acetylcysteine (NAC)³⁶. Yet, the impact of this oxidative stress on the Ca²⁺ handling properties of the t-system remain unclear. In skeletal muscle, the t-system relies on (1) plasma membrane CaATPases (PMCA) over the Na⁺-Ca²⁺-exchanger (NCX) to extrude Ca²⁺ into the t-system lumen because the PMCA is sensitive to the range of [Ca²⁺]_{IS} in the resting fibre and (2) store-operated Ca²⁺ entry (SOCE), providing an extracellular Ca²⁺ influx in response to near-membrane SR Ca²⁺ depletion caused by RyR1 Ca²⁺ leak^{23,37}. These processes may be prone to oxidation^{38,39} playing a potential role in the preservation of fibre Ca²⁺ content⁴⁰.

We assessed both mechanisms (Ca²⁺ extrusion and SOCE) in psoas and TA fibres from WT and Blaj mice by tracking [Ca²⁺]_{t-sys} (t) during a series of internal solution exchanges that depleted and refilled the SR and t-system of Ca²⁺ (Fig. 5a, b). First, fibres were exposed to 30 mM caffeine in a 0 Ca²⁺ solution to deplete the SR of Ca²⁺ and chronically activate SOCE, depleting [Ca²⁺]_{t-sys}⁴¹. Then, fibres were exposed to 60 nM [Ca²⁺]_{cyto} in the presence tetracaine. Inclusion of tetracaine provided a defined [Ca²⁺]_{IS} to assess PMCA activity bypassing any RyR1 leak-dependent increase in the local [Ca²⁺]_{cyto} at the t-system membrane. Therefore, the response of PMCA to a known [Ca²⁺]_{cyto} could be compared across genotypes. Exposure to 60 nM Ca²⁺ activated PMCA, increasing [Ca²⁺]_{t-sys} to a steady state of ~0.6 mM [Ca²⁺]. After this, SOCE was chronically activated by releasing the SR Ca²⁺ with caffeine while continuously imaging [Ca²⁺]_{t-sys}. The imaging rate for this experiment (3.42 frames per second, fps), allowed the determination of the rate of PMCA-mediated Ca²⁺ extrusion and SOCE (Fig. 5c–f).

Both SOCE and Ca²⁺ extrusion were comparable between WT and Blaj fibres from TA. In contrast, Blaj psoas fibres displayed a slower rate of Ca²⁺ extrusion and SOCE compared to WT psoas (Fig. 5g–j). To assess whether this impairment in Blaj psoas fibres was dependent on oxidative stress³⁶, we pre-exposed intact Blaj psoas fibres to the antioxidant N-acetylcysteine (NAC) for 20 min and measured the t-system Ca²⁺ handling properties as shown in Fig. 5a, b. NAC restored the rates of t-system Ca²⁺ extrusion and SOCE to values comparable to those obtained in WT psoas fibres (Fig. 5g, h). Our results show that in dysferlin-deficient psoas, oxidation of t-system Ca²⁺ handling proteins hinders Ca²⁺ fluxes across the t-system membrane.

In skeletal muscle, SOCE is supported by STIM and Orai proteins interacting at the junctional membranes^{42,43}. This facilitates the activation of Ca²⁺ influx immediately upon activation of SR Ca²⁺ depletion^{44,45}. To test whether oxidation also impaired the rapid activation of SOCE (i.e., the coupling between SR Ca²⁺ depletion and extracellular Ca²⁺ influx), caffeine-induced t-system Ca²⁺ depletion was monitored at 27 fps in psoas WT and Blaj fibres simultaneously (Fig. 5i, j; Supplementary movie 2). The WT fibre provided a reference

for observing any shift in the activation kinetics of SOCE in the Blaj fibre. SOCE activation threshold was defined as the time for rhod-5N signal in each fibre to reach a standardized score of -3 (relative to their own baseline) following caffeine exposure. The delay in SOCE activation in Blaj compared to WT was determined by calculating the difference in SOCE activation onset times between Blaj and WT fibres (Fig. 5k).

To account for any potential intragenotype variability among fibres, we compared the delay observed in Blaj vs WT fibres against the delay observed in a WT vs WT fibre setting. A greater delay in SOCE activation lag time following caffeine exposure was detected between Blaj and WT fibres (431.7 ± 233.3 ms) than the WT fibres (194.7 ± 186.2 ms) ($p < 0.01$) (Fig. 5l). This indicates that the absence of dysferlin leads to a delay of ~200 ms in the activation of SOCE in Blaj psoas.

Next, we assessed whether the lag in SOCE activation was due to an impairment of the SOCE mechanism or because of differences in RyR1 Ca²⁺ release activation in response to caffeine. For this, we simultaneously tracked SR Ca²⁺ depletion by imaging SR-trapped fluo-5N under the same conditions as performed in Fig. 5i. We did not observe differences in SR Ca²⁺ depletion kinetics between the genotypes (Fig. 5m–o). In Fig. 5p, the activation delay of SR depletion and SOCE in Blaj relative to WT is compared. This shows that the SOCE impairment observed in the Blaj psoas is not due to a defect in SR calcium release, suggesting a disruption in the SOCE mechanism itself.

To investigate the potential effect of oxidation on this coupling mechanism, we employed a 3-fibre experiment with all fibres containing t-system-trapped rhod-5N (Fig. 5q). A WT fibre provided the reference for standard SOCE activation and was positioned between two Blaj fibres. One of the Blaj fibres was pre-exposed to NAC, while the other was not. SOCE activation was induced by caffeine exposure while imaging at 20 fps (Fig. 5r, s). The NAC-exposed Blaj fibre exhibited a shortened time for SOCE activation following caffeine exposure compared to the untreated Blaj fibre (Fig. 5t) ($p < 0.05$). Collectively, these findings underscore that muscles lacking dysferlin and featuring leaky RyR1s display impaired t-system Ca²⁺ fluxes, as well as delayed SOCE onset upon SR Ca²⁺ depletion due to oxidation.

Oxidation promotes age-dependent progression of LGMD2B/R2

In Blaj psoas there is a clear pathology progression from 8 to 36 weeks-old (Fig. 1). Due to the high load of mitochondrial and cytoplasmic Ca²⁺ in the Blaj psoas, we suspected that ROS (Fig. 4) may have a compounding effect by oxidizing the already phosphorylated RyR1s, exacerbating RyR1 Ca²⁺ leak with age. This would also skew the distribution of fibre Ca²⁺ content further away from the healthy condition¹³. To analyse how the Ca²⁺-handling properties progress with age, we analysed RyR1 Ca²⁺ leak, t-system Ca²⁺ handling and the fibre Ca²⁺ content distribution in 36 weeks-old TA and psoas.

We observed a modest effect of the RyR1 blocker tetracaine on [Ca²⁺]_{t-sys} from both WT and Blaj TA fibres, indicating that RyR1 Ca²⁺ leak was negligible (Fig. 6a). In contrast, tetracaine decreased [Ca²⁺]_{t-sys} in 36-weeks-old WT psoas, comparable to the younger WT psoas (Fig. 1g–i), indicating that in WT, RyR1 Ca²⁺ leak remains higher in psoas than in TA at 36 weeks of age (Fig. 6b, left).

The 36 weeks-old Blaj psoas fibres, however, exhibited a distinct response to RyR1 inhibition. Instead of decreasing the [Ca²⁺]_{t-sys}, RyR1 inhibition increased [Ca²⁺]_{t-sys}, more noticeably as [Ca²⁺]_{cyto} was increased (Fig. 6b). A similar response was previously observed in human muscle with leaky RyR1 gain-of-function variants and concluded to be due to chronic-low conductance SOCE activated by leaky RyR1s²³ (see Methods). To confirm that the tetracaine-induced increase in [Ca²⁺]_{t-sys} was due to SOCE inhibition, we tested the effect of tetracaine in [Ca²⁺]_{t-sys} in the absence and presence of the Orai1 inhibitor BTP2 at a concentration (5 μM) that does not affect RyR1 activity⁴⁶. Figure 6c presents the effects of tetracaine and BTP2 on [Ca²⁺]_{t-sys}

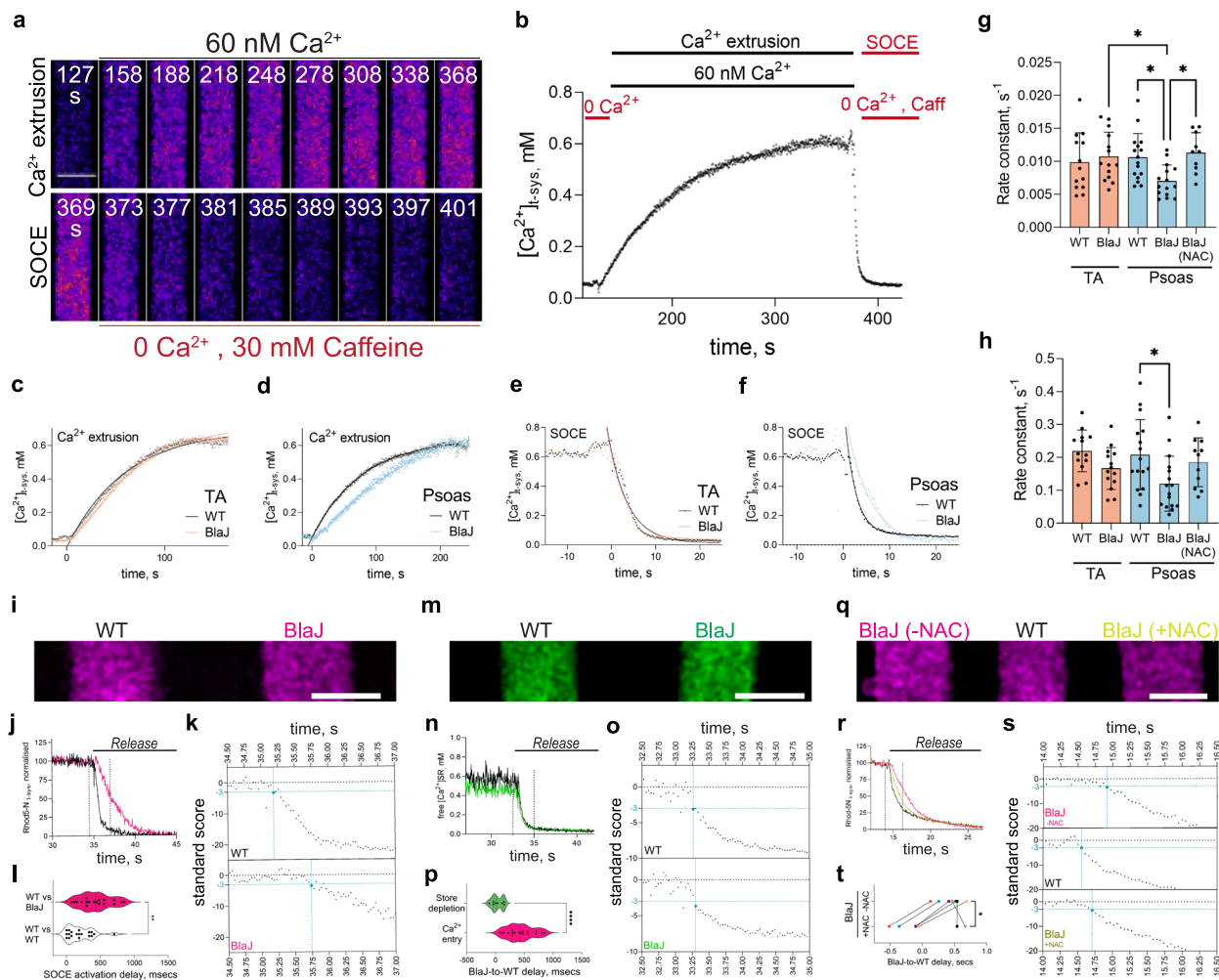


Fig. 5 | Lack of dysferlin drives oxidation-dependent t-system Ca^{2+} handling changes in a muscle-specific fashion. **a** T-system-trapped rhod-5N signal over time during fibre Ca^{2+} extrusion and SOCE. **b** $[\text{Ca}^{2+}]_{\text{t-sys}}(t)$ profile from fibre displayed in **(a)**. **c, d** Representative Ca^{2+} extrusion transients from 8 w/o WT and BlaJ TA (**c**) and psoas (**d**) fibres. **e, f** Representative SOCE transients from 8 w/o WT and BlaJ TA (**e**) and psoas (**f**) fibres. (**c–f**) transients are superposed for visual comparison). **g** Summary of Ca^{2+} extrusion rate constants derived from exponential fitting. **h** Summary of SOCE rate constants derived from exponential fitting. **i** Rhod-5N_{t-sys} confocal image of two psoas fibres (WT and BlaJ) positioned in parallel. **j** Rhod-5N profile from WT (black) and BlaJ (magenta) psoas fibre during exposure to 30 mM caffeine and calcium removal (release solution). **k** transients shown in **(j)** on an expanded timescale. Rhod-5N signal converted to standard score values derived from 5 s baseline. **l** Summary of experiments presented in **(k)**. Delay in SOCE activation; comparison between BlaJ vs WT ($n = 18$) against WT vs WT fibres ($n = 19$).

m Fluo-5N_{SR} confocal image of two psoas fibres (WT and BlaJ) positioned in parallel. **n** Real-time $[\text{Ca}^{2+}]_{\text{SR}}$ in WT (black) and BlaJ (green) psoas fibre during exposure to release solution. **o** transients shown in **n** on an expanded timescale. Fluo-5N signal converted to standard score values derived from 5 s of baseline. **p** Comparison of BlaJ-to-WT delay in SR depletion (**o**) ($n = 8$) vs Ca^{2+} entry ($n = 18$) (**k**). **q** Rhod-5N_{t-sys} confocal image of three fibres (BlaJ, WT and BlaJ (NAC)) positioned in parallel. **r** Rhod-5N profile from WT (black) and BlaJ (pink, -NAC; yellow, +NAC) psoas fibres during exposure to release solution. **s** transients shown in **r** on an expanded timescale. **t** Summary of experiments shown in **(s)** ($n = 15$). SOCE activation threshold in WT served as reference value to define the effect of NAC on BlaJ-to-WT SOCE activation delay. Frame acquisition: 37 fps (**j, n**), 20 fps (**r, l, m, q**). Scale bar: 100 μm . Statistical analysis: (**g, h**), one-way ANOVA with Tukey's multiple comparison. **l, p** Unpaired t-test. (**t**), paired t-test. **** $p < 0.0001$, ** $p < 0.01$, * $p < 0.05$. Source data are provided as a Source Data file.

transients in BlaJ psoas fibres. The strong effect of tetracaine to raise $[\text{Ca}^{2+}]_{\text{t-sys}}$ in the presence of $1.3 \mu\text{M}$ $[\text{Ca}^{2+}]_{\text{cyto}}$ was initially observed. Caffeine was then applied to open and release the RyR1 of tetracaine. The secondary application of $1.3 \mu\text{M}$ $[\text{Ca}^{2+}]_{\text{cyto}}$ was done in the presence of BTP2 and a similar $[\text{Ca}^{2+}]_{\text{t-sys}}$ is achieved to the previous measurement of $[\text{Ca}^{2+}]_{\text{t-sys}}$ in the presence of $1.3 \mu\text{M}$ $[\text{Ca}^{2+}]_{\text{cyto}}$ with tetracaine, consistent with both conditions inhibiting SOCE. In the presence of BTP2, tetracaine lowered $[\text{Ca}^{2+}]_{\text{t-sys}}$ indicating that leak through the RyR1 of BlaJ psoas is increased with age, increasing the Ca^{2+} conductance of Orail channels in the resting muscle (Fig. 6d, e).

To test whether the leak of Ca^{2+} through the RyR1 in 36-week-old BlaJ psoas fibres was exacerbated due to oxidation, we treated intact fibres with NAC before mechanically skinning. In contrast to the previous experiments (in absence of NAC), tetracaine decreased

$[\text{Ca}^{2+}]_{\text{t-sys}}$ (Fig. 6f), indicating that the RyR1s of the 36 weeks-old psoas BlaJ fibres display exacerbated oxidation-dependent leakage, leading to a chronic activation of low amplitude SOCE in the resting muscle. Consistent with this, the ratio of oxidised over reduced RyR1 peptides was increased in 36 weeks-old BlaJ psoas compared to 8 weeks-old BlaJ psoas, a trend that was not observed in the WT groups (Fig. 6g; Supplementary Table 9).

Considering the exacerbated RyR1 Ca^{2+} leak of the aged BlaJ psoas fibres, we measured the distribution of fibre Ca^{2+} content across all muscle groups at both ages (as performed in Fig. 3). In the WT groups, there was no significant change in SR or mitochondrial Ca^{2+} content compared to the younger mice (Fig. 6h, Supplementary Figure 5). In contrast, 36 weeks-old BlaJ presented a reduction in SR Ca^{2+} content compared to 8 weeks-old fibres in both the TA (1.11 ± 0.04 vs

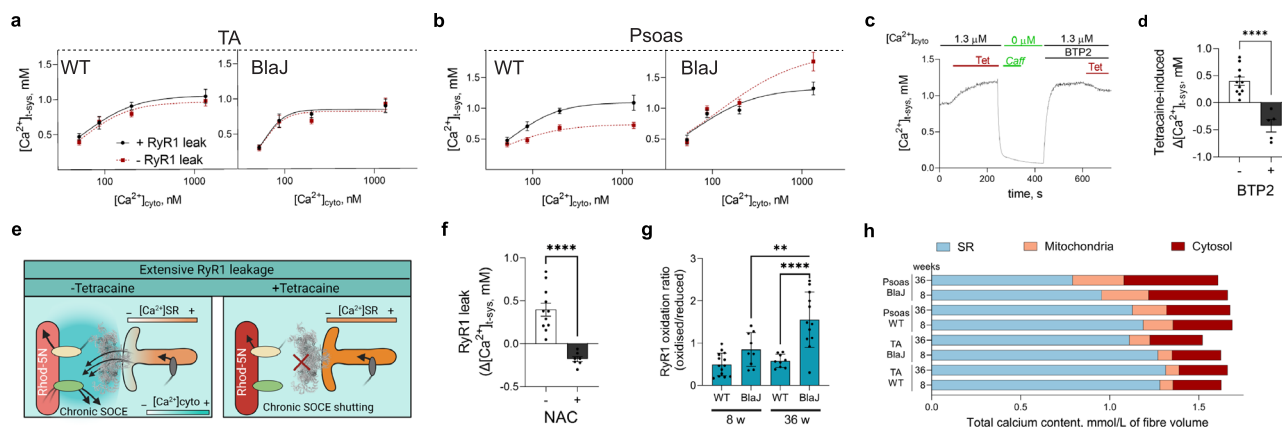


Fig. 6 | Lack of dysferlin drives age-dependent, muscle-specific Ca^{2+} -handling alterations. **a, b** Steady-state $[\text{Ca}^{2+}]_{\text{t-sys}}$ in 36 weeks-old TA and psoas fibres across a range of $[\text{Ca}^{2+}]_{\text{cyto}}$ in presence (black) and absence (red) of RyR1 leak. **c** 36 weeks-old BlaJ psoas $[\text{Ca}^{2+}]_{\text{t-sys}}$ (t) showing the effect of tetracaine on $[\text{Ca}^{2+}]_{\text{t-sys}}$ in absence and presence of BTP2 (5 mM). **d** Effect tetracaine on $[\text{Ca}^{2+}]_{\text{t-sys}}$ in absence and presence of BTP2. Data is presented as Mean \pm SEM. $n = 5-11$. **e** Diagram displaying relationship between RyR1 leak and chronic SOCE observed in 36 weeks-old BlaJ psoas fibres. Upon extensive RyR1 leak, chronic SOCE is activated. Inhibition of this leak inactivates chronic SOCE, leading to accumulation of Ca^{2+} in the t-system. **f** Effect of

N-acetyl cysteine (NAC) on RyR1 leak of 36 weeks-old BlaJ psoas fibres. $n = 7-11$. **g** Ratio of oxidized/reduced RyR1 peptides in psoas. Data derived from data-dependent acquisition MS (Supplementary Table 9). **h** Endogenous Ca^{2+} content (per fibre volume) of the major subcellular compartments in 8 and 36-weeks-old WT and BlaJ TA and psoas fibres, shown as cumulative histograms. (see Supplementary Figure 5). Statistical analysis in **d** and **f** were performed with an unpaired T-test. **** $p < 0.0001$. Statistical analysis in **g** were performed with a one-way ANOVA with Tukey's multiple comparison. Source data are provided as a Source Data file.

1.27 ± 0.06 , $p < 0.0001$) and psoas (0.79 ± 0.04 vs 0.95 ± 0.05 , $p < 0.0001$) muscles. While this decrease was expected in psoas in association with the increased RyR1 Ca^{2+} leak at 36 weeks of age, no increase in leak was observed in TA fibres. This apparent discrepancy may simply reflect a difference in resolution of the respective techniques used to measure RyR1 Ca^{2+} leak and SR Ca^{2+} content.

The mitochondrial Ca^{2+} content in the BlaJ TA and psoas showed a trend towards an increase with age, but this was not significant. The further drop in SR Ca^{2+} content and increase in RyR1 leak in BlaJ fibres without an increase in mitochondrial Ca^{2+} content indicates a plateau has been reached in this latter parameter. For a discussion of this point, see Ref. 32. Together, Fig. 6 shows that the oxidation of already leaky RyR1s in BlaJ psoas exacerbates leak and induces chronic SOCE, resulting in a further skewing of fibre Ca^{2+} distribution.

Discussion

The progression of LGMD2B/R2 in distinct body regions, with dysferlin being absent across all muscle groups, suggests that regional differences unrelated to dysferlin synergistically combine with the absence of dysferlin to underlie disease progression. We have identified that the healthy muscles exhibit differences in RyR1 Ca^{2+} leak that underlie their thermogenic capacity, where psoas, located closer to the body core exhibits a greater leak than the distal muscles examined. The phosphorylation of the RyR1 of psoas and its subsequent increased RyR1 Ca^{2+} leak in both healthy and dysferlin-deficient muscle are hallmarks of muscle-based thermogenesis^{17,18,26}. Here, we find that the phosphorylated and leaky RyR1 of the dysferlin-deficient psoas leads to exacerbation of RyR1 leak, changes in t-system Ca^{2+} permeability via oxidation, SR Ca^{2+} depletion and accumulation of cytoplasmic and mitochondrial Ca^{2+} , events that precede the dystrophic phenotype. We conclude that chronic RyR1 Ca^{2+} leak is a feature in dysferlin-deficient muscles that differentiates the progression of pathology.

We propose that the chronically increased RyR1 Ca^{2+} leak and the resultant redistribution of fibre Ca^{2+} content among the SR, cytoplasm, and mitochondria (Figs. 1 & 3) is critical in triggering the regional progression of pathology in LGMD2B/R2. We also show that the PMCA and proteins regulating SOCE, as well as the RyR1 had their respective functions altered by oxidation, indicating an amplification of ROS generation in the psoas of BlaJ mice as Ca^{2+} accumulated in the

cytoplasm and mitochondria⁴⁷. Notably, the modification of PMCA activity in this context likely contributes to cytosolic and mitochondrial Ca^{2+} increases in BlaJ psoas compared to TA, as the capacity of the cell to clear elevated $[\text{Ca}^{2+}]_{\text{cyto}}$ is reduced. We highlight here that although this ROS-mediated mechanism may offer short-term benefits to the fibres, adapting to reductions in SR Ca^{2+} content for force generation, chronically elevated ROS and $[\text{Ca}^{2+}]_{\text{cyto}}$ are likely underlying factors contributing to pathology.

The stabilization of RyR1 Ca^{2+} leak by nifedipine in BlaJ psoas (Fig. 2) indicates that dysferlin normally provides a stabilizing effect within the t-system membrane to assist the resting DHPR-RyR1 interaction^{9,10}. This aligns with previous observations of (i): a reduced voltage-induced Ca^{2+} transient in dysferlin-null fibres subjected to stress¹¹ and (ii) alleviation of muscle pathology in human LGMD2B/R2 cultured myobundles upon RyR Ca^{2+} leak inhibition⁴⁸. Importantly, these results show consistency across data obtained from mechanically skinned fibres, enzymatically dissociated fibres¹¹ and cultured myofibres⁴⁸, supporting the role of RyR Ca^{2+} leak likely underlying atrophic signalling (leading to the fat and fibrosis accumulation) that characterizes the decline in muscle force observed in LGMD2B/R2⁴⁹. Noteworthy, the stabilizing effect of nifedipine on RyR1 leak to similar levels as the WT occurred even despite a trend of increased RyR1 phosphorylation in BlaJ compared to WT.

Importantly, the lipid composition of the t-system membrane differs between BlaJ and WT fibres^{50,51}. An increase in cholesterol content of the t-system membrane in BlaJ could be a compensatory mechanism to stabilize the physical and functional properties of the membrane in the absence of dysferlin^{46,52,53}. The lack of RyR1 leak exacerbation in BlaJ TA may indicate that the altered t-system lipid environment^{50,51} is sufficient to preserve the inhibitory control of the DHPR on the RyR1 leak in the presence of relatively low RyR1 phosphorylation.

We must also consider that the gastrocnemius muscle, which sits outside the limb girdle, also shows pathology in human LBMD2B/R2, but not in mouse. The biomechanical differences in the walking gait of mouse and human see more stress exerted on the human gastrocnemius compared to mouse. Since mechanical stress on the muscle triggers changes in Ca^{2+} -handling in dysferlinopathy^{11,54}, the extent of muscle excursion during walking may be sufficient to significantly

increase RyR Ca^{2+} leak in the absence of dysferlin in human⁵⁵. Importantly, this possible explanation of the initiation of dysferlinopathy at the gastrocnemius of human does not discount the hypothesis that the thermogenic properties of the muscles at the core of the body underlie the progression of dysferlinopathy at the limb girdle. The suggestion that mechanical stress can initiate dysferlinopathy at the human gastrocnemius is consistent with dysferlin-deficient muscle being intolerant of multiple physiological stresses.

Ca^{2+} handling at the junctional membranes

In the aged Blaj psoas fibres, we observed a leaky RyR1 that triggered a dominant SOCE over Ca^{2+} extrusion by PMCA. An equivalent block of SOCE could be achieved by either inhibiting the RyR1 leak or Orai1 Ca^{2+} influx (Fig. 6). This result confirms that the spatial distribution and molecular components for RyR1 leak-SOCE coupling are the t-system membrane Orai1 conducting the influx of Ca^{2+} via direct coupling from STIM1, positioned to detect the SR terminal cisternae near-membrane luminal Ca^{2+} gradients generated by the leaky RyR1^{37,42–44,56,57}.

Previously we have shown that chronic RyR1 Ca^{2+} leak increases t-system membrane Ca^{2+} permeability, where the RyR1 promotes an increased inward Ca^{2+} flux simultaneously with an increased PMCA activity. These changes compensate for the decrease in SR Ca^{2+} content caused by leaky RyRs by increasing the bulk resting $[\text{Ca}^{2+}]_{\text{cyto}}$ ¹³. In this study, a departure from the expected increase in these t-system Ca^{2+} flux rates were observed in Blaj psoas (Fig. 5). Despite the unexpected impairment in SOCE and PMCA fluxes, the resting bulk $[\text{Ca}^{2+}]_{\text{cyto}}$ increased. This is supported by the mitochondrial Ca^{2+} content being increased significantly (Figs. 3 & 6), which is a function of resting bulk $[\text{Ca}^{2+}]_{\text{cyto}}$ in muscle^{13,32}. We propose that the net increase in the inward Ca^{2+} permeability, necessary to elevate the bulk $[\text{Ca}^{2+}]_{\text{cyto}}$, is reflected by the ratio between the SOCE flux and the PMCA extrusion flux, regardless of the individual fluxes collectively becoming either faster or slower.

In Blaj psoas at early stages of the pathology, generation of ROS occurs due to the accumulation of Ca^{2+} in the cytosol and mitochondria. Oxidation of the PMCA and either or both of Orai1 and STIM proteins causes the mutual slowing of the bidirectional fluxes (Fig. 4). Compounding oxidation of the RyR1 and subsequent accumulation of cytosolic Ca^{2+} due to both increased RyR1 leakage and impaired PMCA activity may be significant factors that underlie the onset and progression of pathology.

We have also shown here that SOCE activation following SR Ca^{2+} release is delayed due to oxidation of the SOCE proteins (Fig. 4). We introduce the term SOCE miscoupling to describe this extended delay between Ca^{2+} release and SOCE. The delay in activation of SOCE may be another important compensatory mechanism to slow the influx of Ca^{2+} to the cytosol, tuning the $[\text{Ca}^{2+}]_{\text{cyto}}$ to the required level. Taken together, these results reveal feedback across the t-system-SR-mitochondrial axis to maintain Ca^{2+} homeostasis in the presence of a leaky RyR1, decreased SR Ca^{2+} content and an altered t-system Ca^{2+} handling function.

The response to cold in core and distal muscles

In endothermic animals such as the mouse, minimising heat loss is critical to saving energy. It follows that generating heat close to the internal organs where it is most needed is more efficient than transporting heat from the distal limbs for the same purpose. The chronic sympathetic activation, RyR1 phosphorylation and increased leak in WT psoas measured here represent a response to a cold challenge, as mice were housed at room temperature, which is below thermoneutrality for this animal. This being the case would support the functional divergence of psoas relative to TA as a muscle specialized for heat generation. As Ser2844 of the RyR1 is a target of protein kinase A, and this kinase is activated by adrenergic signalling, our results suggest that the sympathetic nervous system coordinates the

thermogenic capacity of regions of muscles regulates the thermogenic capacity in a muscle and region-specific fashion.

Here we have shown that the RyR1 Ca^{2+} leak is locally regulated, likely for the purpose of meeting the thermogenic need of regions of the body. Specifically, the body core is surrounded by muscles of higher thermogenic capacity under cold stress⁵⁸. A leaky RyR1 of core compared to distal muscles is carried in dysferlin-deficient muscle. However, we discovered that dysferlin is important for the stabilization of the DHPR and its inhibitory control of the RyR1 resting state. The combination of reduced DHPR inhibitory control and RyR1 phosphorylation of the psoas critically destabilizes the RyR1, exacerbating its leakage prior to the onset of pathology. The resulting redistribution of fibre Ca^{2+} content causes the cytoplasm and mitochondria to accumulate Ca^{2+} and generate ROS. This results in oxidation of the Ca^{2+} handling proteins at the junctional membranes and further increase of RyR1 leak in pathologic dysferlin-deficient muscle.

Methods

Animals

All experimental procedures were approved by the Animal Ethics Committee at the University of Queensland and the study abides by the ARRIVE guidelines for reporting of animal experiments. Male C57BL/6J (WT parental control strain) and Blaj (*dysf*^{−/−}) mice were purchased from Ozgene Australia and housed in groups of 4 mice per cage with standard chow food and water *ad libitum* and maintained in a 12-hour light/dark schedule at room temperature (23 °C). Mice were euthanized by cervical dislocation at 8 and 36 weeks of age and their TA, EDL and psoas muscles were rapidly excised.

RyR1 Ca^{2+} leak and t-system Ca^{2+} handling measurements

Both RyR1 Ca^{2+} leak and t-system Ca^{2+} handling was assessed in single muscle fibres via rhod-5N salt trapped within the compartmentalized transverse tubular (t-) system⁴¹. Briefly, tibialis anterior, EDL, and psoas fibres were isolated under paraffin oil and exposed for 2 min to a “Rhod-5N-external solution” containing (in mM) Rhod-5N, 2.5; CaCl_2 , 2.5; NaCl, 132; MgCl_2 , 1; KCl, 3.3; Hepes, 20 (pH 7.4), using a 2 μL microcapillary tube. Subsequently, the fibres were mechanically skinned using #5 jewellery forceps. This leads to the sealing of the transverse tubules at their mouths, trapping the dye inside this newly generated compartment. Skinned fibres were transferred to a custom-made chamber containing a K^+ -based internal solution (EGTA, 50 mM; ATP, 8 mM; creatine phosphate, 10 mM; Hepes, 90 mM; Na^+ , 36 mM; K^+ , 126 mM; Mg^{2+} , 1 mM; and n-benzyl-p-toluene sulphonamide (BTS), 0.05 mM). $[\text{Ca}^{2+}]$ in the internal solution was set at 0, 28, 52, 87, 200 or 1342 nM. Internal solutions were prepared and $[\text{Ca}^{2+}]$ calculated as described⁵⁹. 50 mM EGTA was used in all internal solutions to heavily buffer the bulk cytoplasmic $[\text{Ca}^{2+}]$. This assists in setting a difference in $[\text{Ca}^{2+}]_{\text{cyto}}$ and $[\text{Ca}^{2+}]_{\text{js}}$, which is critical for measuring RyR Ca^{2+} leak^{13,23,60}. The presence of BTS kept type II fibres from contracting in higher $[\text{Ca}^{2+}]_{\text{cyto}}$, allowing type I fibres to be identified by the presence of contractile protein movement under these conditions. Proteomic analysis showed that the muscles used here were each > 90 % type II fibres (Supplementary Figure 6). To induce a thorough SR Ca^{2+} depletion, fibres were exposed to a “release” internal solution, which was a K^+ -based internal solution where $[\text{Mg}^{2+}]$ was lowered from 1 to 0.01 mM, no Ca^{2+} was added, and 30 mM caffeine was added.

Rhod-5N was excited with the 543-nm line of a HeNe laser, and the emission was filtered using a spectral detector. Depending on the specific experiment, the fibres were imaged using either an Olympus FV1000 or a Leica SP8 confocal microscope, with a 20 \times or 40 \times Plan-Apochromat objective. Unless otherwise stated, the long axis of the image was parallel to the preparation.

For RyR1 leak experiments, rhod-5N images were continuously recorded in *xyt* mode with an aspect ratio of 256 \times 512. Each *xy* frame was captured every 0.8 s. In t-system Ca^{2+} handling experiments, rhod-

5N images were continuously recorded in *xyt* mode with an aspect ratio of 512×128 . Frames were captured every 0.29 s. For high temporal resolution real-time comparisons of SOCE, two or three fibres were placed in the same chamber ~50 microns apart from one another. Rhod-5N images were recorded in *xyt* mode with an aspect ratio of 256×128 , with the long aspect of the image perpendicular to the preparations. Frames were captured every 37 (two fibres) or 51 msec (three fibres). T-system rhod-5N fluorescence (*t*) was collected from each fibre present in the chamber during *xyt* imaging across multiple internal solution changes.

At the conclusion of the experiment, ionomycin (derived from *Streptomyces conglobatus*) and 5 mM Ca^{2+} were applied to each fibre to obtain the fluorescence maximum (F_{\max}), followed by a solution devoid of Ca^{2+} to obtain the minimum (F_{\min}). These values, along with the previously determined $K_{D,\text{Ca}}$ of rhod-5N in the t-system of 0.8 mM⁴¹, were used to determine the $[\text{Ca}^{2+}]_{\text{t-sys}}$ using the following relationship:

$$[\text{Ca}^{2+}]_{\text{t-sys}}(t) = K_{D,\text{Ca}} * [F(t) - F_{\min}] / [F_{\max} - F(t)]. \quad (1)$$

Analysis of $[\text{Ca}^{2+}]_{\text{t-sys}}$ measurements for estimating RyR Ca^{2+} leak

To detect RyR Ca^{2+} leak with t-system-trapped rhod-5N, fibres were exposed to a $[\text{Ca}^{2+}]_{\text{cyto}}$ in the range 28–1342 nM. Following equilibration to the applied $[\text{Ca}^{2+}]_{\text{cyto}}$, a solution containing the same $[\text{Ca}^{2+}]_{\text{cyto}}$ and tetracaine was substituted for the one without tetracaine and $[\text{Ca}^{2+}]_{\text{t-sys}}$ was given enough time to reach a new steady state, which is when the t-system Ca^{2+} uptake equals t-system Ca^{2+} leak. The difference between the steady state $[\text{Ca}^{2+}]_{\text{t-sys}}$ in the absence and presence of tetracaine ($\Delta[\text{Ca}^{2+}]_{\text{t-sys}}$) is the indicator of the RyR Ca^{2+} leak.

When $\Delta[\text{Ca}^{2+}]_{\text{t-sys}}$ becomes more positive, it indicates RyR leak increased. For this to occur, the contribution of RyR Ca^{2+} leak to the junctional space must have caused the $[\text{Ca}^{2+}]_{\text{js}}$ increase to activate the t-system PMCA to move more Ca^{2+} into the t-system lumen than under conditions where $\Delta[\text{Ca}^{2+}]_{\text{t-sys}}$ was lower but > 0 . Therefore, RyR Ca^{2+} leak can be concluded to have increased. In these cases, we do not expect significant action of SOCE.

In some cases, $\Delta[\text{Ca}^{2+}]_{\text{t-sys}}$ becomes negative. Because the steady state $[\text{Ca}^{2+}]_{\text{t-sys}}$ is the net outcome of influx and efflux of Ca^{2+} across the t-system membrane, the addition of tetracaine to block the RyR causes the $[\text{Ca}^{2+}]_{\text{t-sys}}$ to rise; this indicates that in the presence of tetracaine a dominant efflux of Ca^{2+} from the t-system lumen has been blocked. The blockade of the RyR Ca^{2+} leak is proposed to stop the near-membrane depletion of Ca^{2+} inside the SR terminal cisternae. This allows STIM1 to bind adequate Ca^{2+} to terminate the SOCE that was causing the dominant efflux of Ca^{2+} across the t-system membrane in the absence of tetracaine. In this study (Fig. 6), the leaky RyR of the aged BlaJ psoas fibres presented this behaviour and the same result to blocking SOCE with a RyR inhibitor was achieved by directly blocking Orai1 with BTP-2. This confirms the origin of the dominant t-system Ca^{2+} efflux was SOCE and that the activation of a dominant SOCE (compared to t-system PMCA Ca^{2+} flux) indicates RyR Ca^{2+} leak was greater than in situations where $\Delta[\text{Ca}^{2+}]_{\text{t-sys}}$ was > 0 .

We note that there is some variability across the $[\text{Ca}^{2+}]_{\text{t-sys}}$ values presented, for example, across Fig. 2. Note that this occurs frequently if comparing fibres from different muscles. This may reflect differences in populations of t-system membrane Ca^{2+} channels and pumps, which must affect the evolution of $[\text{Ca}^{2+}]_{\text{t-sys}}$ and its steady state.

Ca^{2+} content measurements

The intracellular Ca^{2+} content of a fibre was calculated based on the force elicited by the fibre in response to membrane lysis that releases all compartmentalized Ca^{2+} to the cytoplasm.

First, the total amount of Ca^{2+} contained in a fibre was quantified by pre-equilibrating the skinned fibre in a solution with a known

concentration of the very fast Ca^{2+} -buffer BAPTA and then transferring the fibre to an emulsion of 10% Triton X-100 and paraffin oil (TX-oil) to lyse all membranous compartments and release any Ca^{2+} from within the fibre. The Ca^{2+} released from the different intracellular organelles upon the membrane lysing binds to the known amount of BAPTA present within the fibre and to troponin C (TnC) proteins. The pre-equilibrating [BAPTA] was chosen such that the fibre produced a finite, non-maximal force response upon lysis (in the μM to low mM range); this allowed for the calculation of the total amount of Ca^{2+} present in the fibre in absolute terms considering the [BAPTA] in the equilibration solution and the magnitude of the force response. Other skinned fibre preparations, prior to the TX-oil lysing, were i) fully depleted of their endogenous SR Ca^{2+} content by a 1 min exposure to a full release solution (0 Mg^{2+} + 30 mM Caffeine), or ii) fully depleted of their mitochondrial Ca^{2+} content by exposure to 5 μM FCCP.

Calculation of Ca^{2+} release from lysing experiment:

The total Ca^{2+} content within the fibre at the time of lysis ($[\text{Ca}^{2+}]_{\text{T}}$), expressed in millimoles per litre total fibre volume was calculated as the sum of (i) the Ca^{2+} bound to BAPTA, (ii) the Ca^{2+} bound to all other high affinity binding sites in the fibre (predominantly Troponin C (TnC)). Briefly, the total amount of Ca^{2+} within a given fibre ($[\text{Ca}^{2+}]_{\text{T}}$) was calculated as follows:

1. The cytoplasmic free Ca^{2+} concentration ($[\text{Ca}^{2+}]$, in molar units) within the fibre at the peak of the force response elicited upon lysis was calculated from the relationship between force and $[\text{Ca}^{2+}]$ which was defined as being the Hill curve with values of pCa50 and Hill coefficient for that fibre of the specified mouse group.
2. The effective [BAPTA] within the fibre was taken as being 1.13 times the [BAPTA] of the pre-equilibration solution, to account for the swelling of the fibre when initially placed in solution, and also the fibre volume to which BAPTA was not accessible (i.e., that occupied by the SR, t-tubular system and mitochondria etc.)
3. The percentage of BAPTA with bound Ca^{2+} (%CaBAPTA) was determined from the size of the force response, the relevant force- $[\text{Ca}^{2+}]$ relationship and the known Ca^{2+} -binding properties of BAPTA⁶¹.
4. Ca^{2+} binds to the ATP and HDTA present, and the total of these and the free $[\text{Ca}^{2+}]$ was estimated as being $-9.6 \times [\text{Ca}^{2+}]$.
5. Finally, 0.015 mmol l⁻¹ was deducted from the total to take into account the contaminating Ca^{2+} present in the BAPTA pre-equilibration solution. The total Ca^{2+} content within the fibre at the time of the lysis (expressed in millimoles per liter fibre volume) was thus calculated as:

$$[\text{Ca}^{2+}]_{\text{T}} = 1.13 \times [\text{BAPTA}] \times \% \text{CaBAPTA} / 100 + \text{CaTnC} + 9.6 \times [\text{Ca}^{2+}] \times 1000 - 0.015 \quad (2)$$

N-acetylcysteine treatment

To assess the effect of N-acetylcysteine (NAC) in t-system Ca^{2+} handling, a bundle of (5–20) fibres was isolated under paraffin oil, pinned at resting tension and exposed for 20 min to a “rhod-5N-external solution” (described in *RyR1 Ca^{2+} leak and t-system Ca^{2+} handling measurements* section) containing 2 mM NAC. Following this, single fibres were mechanically skinned and imaged as described above.

Hematoxylin and Eosin staining

TA, EDL and psoas muscles were excised from WT and BlaJ mice at 8 and 36 weeks of age and cut in half transversely across the belly of the muscle. Samples were fixed (4% paraformaldehyde (PFA) in phosphate buffer solution (PBS)) overnight at 4 °C and washed in running water for 20 min.

Washed samples were progressively incubated through 70, 90 and 100% ethanol solutions for 45 min each. The samples were then

covered in xylene for 45 min. Finally, muscles were covered in wax for 45 min at 60 °C before wax immersion. Embedding was performed resting the belly-side of each sample at the bottom of the chamber. 0.25 microns depth cross sections were obtained using a Leica RM2245 semi-automated rotary microtome and mounted into 40 × 24 mm slides.

Samples went through brief (1 min) incubations in Xylene followed by absolute ethanol prior to incubation in Hematoxylin for 2 min. Afterwards, the samples were washed in running water for 5 min and exposed to Eosin for 0.5 min. This was followed by exposure to increasing concentrations of ethanol (70, 90 and 100%, 1 min per ethanol concentration). Finally, 3 consecutive 1-minute incubations with xylene were performed. Images were obtained with an Aperio XT Brightfield Slide Scanner at least 24 h after the staining was performed.

Proteomic analysis

Reagents and consumables. Trifluoroacetic acid, dithiothreitol, iodoacetamide, ammonium bicarbonate, formic acid, acetonitrile and trypsin (MS grade) were purchased from Sigma-Aldrich. C18 ZipTips were from Millipore. 10 kDa cut-off Ultra devices were from Amicon.

Tissue lysis. Mouse TAs and psoas (2 mg) were finely diced and resuspended in 60 µl of trifluoroacetic acid (TFA) in Eppendorf tubes. The mixtures were incubated at room temperature with frequent vortexing. During tissue lysis, the volume of TFA in the reaction gradually decreased so it was critical that additional TFA was added to ensure the volume of TFA in the reaction was maintained. Once lysis was complete, samples were neutralized with 2 M Tris Base using 8 × volume of TFA.

Filter aided sample preparation (FASP). To improve MS signal, FASP was used to remove small molecular weight components from muscle homogenates. Each muscle homogenate sample (500 µl) was mixed with 18 µl of 0.5 M dithiothreitol and incubated at 30 °C for 30 min. Following addition of 19 µl of 0.5 M iodoacetamide, the mixture was incubated at 30 °C for 50 min. The reduced and alkylated protein sample was transferred to a 10 kDa cut-off Ultra device which was placed into a collection tube and centrifuged at 14,000 × g for 30 min. The flow through from the column was removed and 200 µl of 100 mM ammonium bicarbonate was added to the column followed by centrifugation at 14,000 × g for 30 min. To digest proteins in the column, 150 µl of 100 mM ammonium bicarbonate containing 2 µg Trypsin was added. The column was incubated at 37 °C for 20 h and then centrifuged in a new collection tube at 18,000 × g for 30 min. 50 µl of 0.1% formic acid was then added to the spin column followed by centrifugation at 14,000 × g for 30 min to elute remaining digested peptides. C18 ZipTips were used to desalt the samples following the manufacturer's instructions and the desalted peptides were eluted with 80% acetonitrile/0.1% formic acid into Eppendorf tubes. Digested peptide samples were dried down using a vacuum concentrator (Concentrator plus, Eppendorf) and reconstituted with 40 µl 0.1% formic acid.

Data dependent acquisition (DDA). Peptides (375 ng) were separated using a Supelco Bioshell peptide C18 160 Å, 2.7 µm, 0.3 × 150 mm column and Eksigent LC415 micro liquid chromatography system before being injected onto a ZenoTOF 7600 mass spectrometer (Sciex, Framingham, MA, USA). Mobile phase buffer A (water with 0.1% formic acid) and buffer B (acetonitrile with 0.1% formic acid) flowed at 5 µL/min on the following 45 min gradient: 3–35% B from 0–39 min, 35–80% B from 39–43 min, then decreasing back to 3% B at 43 min, which was held for the remaining 2 min. Mass spectrometry source parameters were as follows: ion source gas 1 = 20 psi, ion source gas 2 = 15 psi, curtain gas = 35 psi, CAD gas = 7 psi, source temperature = 150 °C and column temperature = 40 °C. TOF MS parameters were as

follows: acquisition range = 400–1500 Da, accumulation time = 0.2 s, declustering potential = 80 v, declustering potential spread = 0 v, collision energy = 10 v, and spray voltage was set to 4800 V. TOF MS/MS parameters were as follows: polarity = positive ionization mode, spray voltage = 4800 v, TOF range = 100–1500 Da, accumulation time = 0.08 s, declustering potential = 80 v, declustering potential spread = 0 v. For fragmentation, a maximum of 20 intense precursor ions per cycle were selected at an intensity threshold exceeding 100 cps. Sample precursor ions were dynamically excluded for 4 s after one incidence of MS/MS sampling occurrence. Precursor ions from charge states 2–5 were selected for fragmentation using collision-induced-dissociation (CID). External calibration was performed every 3 runs using the automatic calibration function and X500 ESI positive calibration solution from SCIEX. Signal stability over time were monitored by repeat injection of 400 ng Hela protein digest (Thermo Fisher Scientific).

SWATH. A SWATH acquisition method with 65 variable-sized windows (Supplementary Table 1) covering a precursor mass range of 140–1750 Da was used. The chromatographic conditions and source conditions were essentially the same used in the DDA run described above. TOF MS scans were done using a mass range of 400–1500 Da with accumulation time of 0.1 s, declustering potential = 80 v, declustering potential spread = 0 v, collision energy = 10 v and collision energy spread = 0 v; spray voltage was set to 4800 v. TOF MS/MS was performed over the mass range 140–1750 Da with accumulation time of 0.013 s and fragmentation mode = collision induced dissociation (CID). External calibration was performed every 3 runs using the automatic calibration function and X500 ESI positive calibration solution from SCIEX. Signal stability over time were monitored by repeat injection of 400 ng Hela protein digest (Thermo Fisher Scientific).

Database search. Product ion spectra were processed using the Paragon search engine on ProteinPilot Software (5.01, AB Sciex, Redwood City, CA) against a curated Mus Musculus Uniprot database (downloaded, 2023) with sequences in forward and reverse orientations. Each raw file from each sample was searched as single input and resulting output file used as ion library for SWATH data processing. Search Parameters were as follows: sample type = identification; cyst alkylation = iodoacetamide; digestion = trypsin; instrument = Triple-TOF 6600; special factors = none; and ID focus = biological modifications and amino acid substitution. False discovery rate (FDR) was selected in the processing method which sets the detected protein threshold to 0.05 (10%).

SWATH analysis. The SWATH data was interrogated against the ion library, using the PeakView software (Sciex, version 1.2.0.3). Marker-View software was then used to review the data to determine the up and down regulation of protein expression in the skeletal muscle samples.

Multiple Reaction Monitoring (MRM). Measurements of phosphorylated and unphosphorylated RyR1 in skeletal muscle samples were performed by MRM. Skyline software (Skyline version 21.2.0.568) was used to generate an MRM-HR method for the ZenoToF 7600 system based on results obtained from the DDA experiment. A total of 25 peptides were added to the ZenoToF 7600 MRM-HR method. Sequences of peptides corresponding to the Titin protein were also included for quality control as it was identified as the major protein in mouse skeletal muscle during the protein identification (DDA) workflow. A 2 µl sample (containing 375 ng of peptides) was injected for analysis. Peptides were separated using a Bioshell peptide C18 160 Å, 2.7 µm, 0.3 × 150 mm column from Supelco. The mobile phase buffer A (0.1% formic acid in water) and buffer B (0.1% formic acid in acetonitrile) flowed at 5 µL/min on the following 20 min gradient: 3–5% B from

0–0.5 min, 5–35% B from 0.5–16 min, 35–80% B from 16–18 min, then decreasing back to 3% B at 18 min, which was held for the remaining 2 min. Samples eluting from the column were monitored in positive ion mode with MRM on a ZenoToF 7600 mass spectrometer with total scan time = 2.929 s, estimated cycles = 410, ionization start time = 3 min and ionization stop time = 15 min. The following ion source parameters were used: ion source gas 1 = 20 psi, ion source gas 2 = 15 psi, curtain gas = 35 psi, CAD gas = 7 psi, source temperature = 150 °C and column temperature = 40 °C. The parameters used for TOF MS were as follows: TOF start mass = 400 Da, TOF stop mass = 1800 Da, accumulation time = 0.05 s, declustering potential = 80 v, declustering potential spread = 0 v, collision energy = 10 v, collision energy spread = 0 v and spray voltage was set to 4800 V. TOF MS/MS scanning used Zeno pulsing with a threshold of 20,000 cps, then scanning from 100–1800 Da; the list of target peptides, precursor ion mass, accumulation time, declustering potential, collision energies, and collision energy spread can be found in Supplementary Table 2. RyR1 peptides (phosphorylated and unphosphorylated) were monitored using the precursor-product ion transitions listed in Supplementary Table 3. Data was normalised against the Total Ion Area observed for each sample and Peak areas were adjusted to reflect these differences. Data from two independent experiments (Exp. 1, $n = 4$; Exp. 2, $n = 3$) were normalised to their respective WT TA group and pooled together. Outliers identified as values 2 SEMs beyond the average of each group were excluded.

Function annotation

For proteomics data analysis, Kyoto Encyclopedia of Genes and Genomes (KEGG) pathway and Gene Ontology (GO) analysis were performed using the Database for Annotation, Visualization, and Integrated Discovery (DAVID) bioinformatics web tool⁶². Enriched terms presented here exhibit an adjusted (Benjamini-Hochberg) P value < 0.05.

Western Blotting

Samples (30 µg) were separated on 4–12% Criterion XT Bis-Tris gels (Bio-Rad) for 1.5 h at 125 V and transferred to nitrocellulose membranes (wet transfer) for 1 h at 100 V. Upon transfer, membranes were stained with Ponceau S solution for 2–5 mins at room temperature and rinsed with distilled water, removing background stain. Ponceau S signal was captured with a Chemidoc System. Thereafter, membranes were blocked (1 h, 5% BSA in tris-buffered saline (TBS) with Tween 20 (TBST)) and incubated overnight with phospho-PKA substrate primary antibody (Cell Signaling, 9624) (1:1000 dilution). Afterwards, membranes were washed 3 times with TBST (5 mins each wash) and incubated with rabbit (1:10,000) secondary antibody for 1 h at RT followed by 3 washes in TBST. Protein bands were visualized with a Chemidoc System after applying chemoluminescent substrate to the membrane. Densitometry was performed using ImageJ and averaged signal between 25 and 140 kDa was normalised to their respective Ponceau S signal.

Norepinephrine quantification

Norepinephrine concentration in muscles was measured according to the kit protocol (Abcam, ab287789). Briefly, cryogenically homogenised muscles were subjected to competitive enzyme-linked immunosorbent assay. Absorbance (450 nm) values were interpolated in a standard curve run in parallel to the experiment.

Metabolomic analysis

To extract polar metabolites, ~50 mg of tissue was cryoground before the addition of zirconium oxide beads (1.4 mm, Precellys, cat. no. KT03961-1-103.BK, ~10 beads per tube) and resuspension with a 1:1 (v/v) mixture of methanol/water, pre-chilled at -20 °C and

supplemented with 1 µM 4-morpholineethanesulfonic acid (Sigma-Aldrich, cat. no. M2933). Samples were then homogenised (3 × 30 sec at 25 Hz) with the Qiagen TissueLyser II before the addition 1 vol of CHCl₃, brief vortexing, and centrifugation for 20 min at 16,000 × g and 4 °C. The supernatant was lyophilised (maximum temperature of 35 °C) using a GeneVac EZ-2 centrifugal evaporator. Blank samples (extraction buffer without any tissue) were processed in parallel as a negative control.

Lyophilised samples were then resuspended in a 1:1 (v/v) mixture of acetonitrile/water with ultra-sonication (4 × 30 sec) and clarified by centrifugation for 20 min at 16,000 × g and 4 °C. The supernatant was subjected to targeted liquid chromatography-coupled mass spectrometry (LC-MS). First, metabolites were resolved by LC using a 1290 Infinity II pump (Agilent) with an InfinityLab Poroshell 120 HILIC-Z column (Agilent, 2.7 µm particle size, 2.1 mm internal diameter × 100 mm length, stainless-steel lined). Buffer A was 80:20 (v/v) acetonitrile/water and Buffer B was 10:90 (v/v) acetonitrile/water, both containing 10 mM ammonium acetate (pH 9) and 5 µM medronic acid (Thermo cat. no. 215070010). The medronic acid was included as an additive to improve sensitivity and reduce peak-tailing⁶³. In conjunction, the column was deactivated with 0.5% (v/v) phosphoric acid prior to use, according to the manufacturer's protocol. The LC gradient was as follows: 0 min, 0% B, 250 µL/min; 2 min, 0% B, 250 µL/min; 12 min, 40% B, 250 µL/min; 14 min, 40% B, 250 µL/min; 14.5 min, 0% B, 500 µL/min; 18.4 min, 0% B, 500 µL/min; 18.5 min, 0% B, 250 µL/min. Autosampler temperature was 4 °C, column temperature was 30 °C, and injection volume was 3 µL. MS analysis was performed using an Agilent 6470 QQQ with Jet Stream Technology Ion Source, with the following parameters: gas temperature at 200 °C, gas flow at 11 L/min, nebuliser pressure at 40 psi, sheath gas temperature at 400 °C, sheath gas flow at 12 L/min, capillary voltage at 3000 V for both negative and positive modes, and nozzle voltage at 0 V for negative mode and 500 V for positive mode. Multiple-reaction monitoring transitions were calibrated and optimised using metabolite standards, with transition parameters available upon request.

LCMS data was extracted using Skyline (version 23.1.0.380-cf25ad847)⁶⁴. Metabolite peak areas were normalised to the internal standard and converted to absolute quantities using the calibration standards.

Mitochondrial membrane potential assessment

To measure mitochondrial membrane potential, pairs of WT TA and psoas fibres were mechanically skinned and imaged simultaneously (~30–50 microns apart) during exposure to 150 nM Tetramethyl rhodamine, Ethyl Ester (TMRE) until a plateau was reached in both fibres. TMRE was excited with a 543 HeNe laser and emission was filtered using a spectral detector. *xyt* imaging was conducted with an Olympus FV1000 (40x Plan-Apochromat objective) every 0.978 s under an aspect size ratio of 320 × 256 pixels. For quantification, TMRE signal from both fibres was normalised to the signal from the TA fibre.

Statistical analysis

Statistical analyses were performed with GraphPad Prism 10. To determine statistical significance, a student's t -test (paired or unpaired, depending on the experimental design and specified in figure legend), one-way ANOVA with Tukey's post-hoc test or a two-way ANOVA with Tukey's post-hoc test was performed. Unless otherwise stated, two-tailed tests were performed. Statistical significance was accepted if $P < 0.05$.

Reporting summary

Further information on research design is available in the Nature Portfolio Reporting Summary linked to this article.

Data availability

All data generated in this study are included in this article. Individual data points included in main figures can be found in Supplementary Data 1. Individual data points included in Supplementary Figs. can be found in Supplementary Data 2. Proteomics data generated have been deposited in ProteomeXChange with PRIDE under accession code PXD056568. Metabolomics data generated have been deposited in Metabolomics Workbench (Project ID: [PR002361](https://doi.org/10.21228/M8FN8H)). The DOI for this project is <https://doi.org/10.21228/M8FN8H>. Source data are provided with this paper.

References

- Argov, Z. et al. Muscular dystrophy due to dysferlin deficiency in Libyan Jews. *Brain* **123**, 1229–1237 (2000).
- Nagy, N. et al. Hip region muscular dystrophy and emergence of motor deficits in dysferlin-deficient Bla/J mice. *Physiol. Rep.* **5**, e13173 (2017).
- Kerr, J. P., Ward, C. W. & Bloch, R. J. Dysferlin at transverse tubules regulates Ca^{2+} homeostasis in skeletal muscle. *Front. Physiol.* **5**, 89 (2014).
- Bansal, D. et al. Defective membrane repair in dysferlin-deficient muscular dystrophy. *Nature* **423**, 168–172 (2003).
- Hofhuis, J. et al. Dysferlin mediates membrane tubulation and links T-tubule biogenesis to muscular dystrophy. *J. Cell Sci.* **130**, 841–852 (2017).
- Ampong, B. N., Imamura, M., Matsumiya, T., Yoshida, M. & Takeda, S. Intracellular localization of dysferlin and its association with the dihydropyridine receptor. *Acta Myol. Myopathies Cardiomyopathies Off. J. Mediterr. Soc. Myol.* **24**, 134–144 (2005).
- Whiteley, G., Collins, R. F. & Kitmitto, A. Characterization of the Molecular Architecture of Human Caveolin-3 and Interaction with the Skeletal Muscle Ryanodine Receptor. *J. Biol. Chem.* **287**, 40302–40316 (2012).
- Zhou, J. et al. A probable role of dihydropyridine receptors in repression of Ca^{2+} sparks demonstrated in cultured mammalian muscle. *Am. J. Physiol.-Cell Physiol.* **290**, C539–C553 (2006).
- Eltit, J. M. et al. Orthograde dihydropyridine receptor signal regulates ryanodine receptor passive leak. *Proc. Natl. Acad. Sci.* **108**, 7046–7051 (2011).
- Eltit, J. M. et al. Malignant hyperthermia susceptibility arising from altered resting coupling between the skeletal muscle L-type Ca^{2+} channel and the type I ryanodine receptor. *Proc. Natl. Acad. Sci.* **109**, 7923–7928 (2012).
- Lukyanenko, V., Muriel, J. M. & Bloch, R. J. Coupling of excitation to Ca^{2+} release is modulated by dysferlin. *J. Physiol.* **595**, 5191–5207 (2017).
- Barefield, D. Y. et al. Loss of dysferlin or myoferlin results in differential defects in excitation–contraction coupling in mouse skeletal muscle. *Sci. Rep.* **11**, 15865 (2021).
- Lambley, C. R. et al. Ryanodine receptor leak triggers fiber Ca^{2+} redistribution to preserve force and elevate basal metabolism in skeletal muscle. *Sci. Adv.* **7**, eabi7166 (2021).
- Place, N. et al. Ryanodine receptor fragmentation and sarcoplasmic reticulum Ca^{2+} leak after one session of high-intensity interval exercise. *Proc. Natl. Acad. Sci.* **112**, 15492–15497 (2015).
- Ivarsson, N. et al. SR Ca^{2+} leak in skeletal muscle fibers acts as an intracellular signal to increase fatigue resistance. *J. Gen. Physiol.* **151**, 567–577 (2019).
- Bal, N. C., Maurya, S. K., Singh, S., Wehrens, X. H. T. & Periasamy, M. Increased Reliance on Muscle-based Thermogenesis upon Acute Minimization of Brown Adipose Tissue Function. *J. Biol. Chem.* **291**, 17247–17257 (2016).
- Meizoso-Huesca, A., Pearce, L., Barclay, C. J. & Launikonis, B. S. Ca^{2+} leak through ryanodine receptor 1 regulates thermogenesis in resting skeletal muscle. *Proc. Natl. Acad. Sci.* **119**, e2119203119 (2022).
- Launikonis, B. S. & Murphy, R. M. From Muscle-Based Nonshivering Thermogenesis to Malignant Hyperthermia in Mammals. *Annu. Rev. Physiol.* <https://doi.org/10.1146/annurev-physiol-022724-105205> (2025).
- Lawal, T. A., Todd, J. J. & Meilleur, K. G. Ryanodine Receptor 1-Related Myopathies: Diagnostic and Therapeutic Approaches. *Neurotherapeutics* **15**, 885–899 (2018).
- Andersson, D. C. et al. Ryanodine Receptor Oxidation Causes Intracellular Calcium Leak and Muscle Weakness in Aging. *Cell Metab.* **14**, 196–207 (2011).
- Waning, D. L. et al. Excess TGF- β mediates muscle weakness associated with bone metastases in mice. *Nat. Med.* **21**, 1262–1271 (2015).
- Potter, R. A. et al. Systemic Delivery of Dysferlin Overlap Vectors Provides Long-Term Gene Expression and Functional Improvement for Dysferlinopathy. *Hum. Gene Ther.* **29**, 749–762 (2018).
- Cully, T. R. et al. Junctional membrane Ca^{2+} dynamics in human muscle fibers are altered by malignant hyperthermia causative RyR mutation. *Proc. Natl. Acad. Sci.* **115**, 8215–8220 (2018).
- Bardsley, O. J., Matthews, H. R. & Huang, C. L.-H. Finite element analysis predicts Ca^{2+} microdomains within tubular-sarcoplasmic reticular junctions of amphibian skeletal muscle. *Sci. Rep.* **11**, 14376 (2021).
- Csernoch, L. et al. Effects of tetracaine on sarcoplasmic calcium release in mammalian skeletal muscle fibres. *J. Physiol.* **515**, 843–857 (1999).
- Singh, D. P. et al. Evolutionary isolation of ryanodine receptor isoform 1 for muscle-based thermogenesis in mammals. *Proc. Natl. Acad. Sci.* **120**, e2117503120 (2023).
- Laver, D. R. Regulation of the RyR channel gating by Ca^{2+} and Mg^{2+} . *Biophys. Rev.* **10**, 1087–1095 (2018).
- Reiken, S. et al. PKA phosphorylation activates the calcium release channel (ryanodine receptor) in skeletal muscle. *J. Cell Biol.* **160**, 919–928 (2003).
- Andersson, D. C. et al. Stress-induced increase in skeletal muscle force requires protein kinase A phosphorylation of the ryanodine receptor. *J. Physiol.* **590**, 6381–6387 (2012).
- Fryer, M. W. & Stephenson, D. G. Total and sarcoplasmic reticulum calcium contents of skinned fibres from rat skeletal muscle. *J. Physiol.* **493**, 357–370 (1996).
- Lambley, C. R., Murphy, R. M., McKenna, M. J. & Lamb, G. D. Sarcoplasmic reticulum Ca^{2+} uptake and leak properties, and SERCA isoform expression, in type I and type II fibres of human skeletal muscle. *J. Physiol.* **592**, 1381–1395 (2014).
- Seng, C. et al. Tiny changes in cytoplasmic $[\text{Ca}^{2+}]$ cause large changes in mitochondrial Ca^{2+} : what are the triggers and functional implications? *Am. J. Physiol.-Cell Physiol.* **323**, C1285–C1289 (2022).
- Zanou, N. et al. Acute RyR1 Ca^{2+} leak enhances NADH-linked mitochondrial respiratory capacity. *Nat. Commun.* **12**, 7219 (2021).
- Williamson, D., Lund, P. & Krebs, H. The redox state of free nicotinamide-adenine dinucleotide in the cytoplasm and mitochondria of rat liver. *Biochem. J.* **103**, 514–527 (1967).
- Christensen, C. E., Karlsson, M., Winther, J. R., Jensen, P. R. & Lerche, M. H. Non-invasive In-cell Determination of Free Cytosolic $[\text{NAD}^+]/[\text{NADH}]$ Ratios Using Hyperpolarized Glucose Show Large Variations in Metabolic Phenotypes. *J. Biol. Chem.* **289**, 2344–2352 (2014).
- García-Campos, P. et al. N-Acetylcysteine Reduces Skeletal Muscles Oxidative Stress and Improves Grip Strength in Dysferlin-Deficient Bla/J Mice. *Int. J. Mol. Sci.* **21**, 4293 (2020).

37. Pearce, L. et al. Ryanodine receptor activity and store-operated Ca^{2+} entry: Critical regulators of Ca^{2+} content and function in skeletal muscle. *J. Physiol.* **601**, 4183–4202 (2023).
38. Zaidi, A. Plasma membrane Ca^{2+} -ATPases: Targets of oxidative stress in brain aging and neurodegeneration. *World J. Biol. Chem.* **1**, 271 (2010).
39. Gibhardt, C. S. et al. Oxidative Stress-Induced STIM2 Cysteine Modifications Suppress Store-Operated Calcium Entry. *Cell Rep* **33**, 108292 (2020).
40. Ríos, E. The cell boundary theorem: a simple law of the control of cytosolic calcium concentration. *J. Physiol. Sci.* **60**, 81 (2010).
41. Cully, T. R., Edwards, J. N., Murphy, R. M. & Launikonis, B. S. A quantitative description of tubular system Ca^{2+} handling in fast- and slow-twitch muscle fibres. *J. Physiol.* **594**, 2795–2810 (2016).
42. Stiber, J. et al. STIM1 signalling controls store-operated calcium entry required for development and contractile function in skeletal muscle. *Nat. Cell Biol.* **10**, 688–697 (2008).
43. Zhang, H. et al. Desmin interacts with STIM1 and coordinates Ca^{2+} signaling in skeletal muscle. *JCI Insight* **6**, e143472 (2021).
44. Edwards, J. N., Blackmore, D. G., Gilbert, D. F., Murphy, R. M. & Launikonis, B. S. Store-operated calcium entry remains fully functional in aged mouse skeletal muscle despite a decline in STIM1 protein expression. *Aging Cell* **10**, 675–685 (2011).
45. Koenig, X. et al. Mechanistic insights into store-operated Ca^{2+} entry during excitation-contraction coupling in skeletal muscle. *Biochim. Biophys. Acta BBA - Mol. Cell Res.* **1866**, 1239–1248 (2019).
46. Meizoso-Huesca, A. & Launikonis, B. S. The Orai1 inhibitor BTP2 has multiple effects on Ca^{2+} handling in skeletal muscle. *J. Gen. Physiol.* **153**, e202012747 (2021).
47. Peng, T. & Jou, M. Oxidative stress caused by mitochondrial calcium overload. *Ann. N.Y. Acad. Sci.* **1201**, 183–188 (2010).
48. Khodabukus, A. et al. Bioengineered Model of Human LGMD2B Skeletal Muscle Reveals Roles of Intracellular Calcium Overload in Contractile and Metabolic Dysfunction in Dysferlinopathy. *Adv. Sci.* **11**, 2400188 (2024).
49. Grounds, M. D. et al. Lipid Accumulation in Dysferlin-Deficient Muscles. *Am. J. Pathol.* **184**, 1668–1676 (2014).
50. Sellers, S. L. et al. Increased nonHDL cholesterol levels cause muscle wasting and ambulatory dysfunction in the mouse model of LGMD2B. *J. Lipid Res.* **59**, 261–272 (2018).
51. Haynes, V. R. et al. Dysferlin deficiency alters lipid metabolism and remodels the skeletal muscle lipidome in mice. *J. Lipid Res.* **60**, 1350–1364 (2019).
52. Launikonis, B. S. & Stephenson, D. G. Effects of membrane cholesterol manipulation on excitation-contraction coupling in skeletal muscle of the toad. *J. Physiol.* **534**, 71–85 (2001).
53. Pouvreau, S. et al. Membrane cholesterol modulates dihydropyridine receptor function in mice fetal skeletal muscle cells. *J. Physiol.* **555**, 365–381 (2004).
54. Lukyanenko, V., Muriel, J., Garman, D., Breydo, L. & Bloch, R. J. Elevated Ca^{2+} at the triad junction underlies dysregulation of Ca^{2+} signaling in dysferlin-null skeletal muscle. *Front. Physiol.* **13**, 1032447 (2022).
55. Hu, X., Charles, J. P., Akay, T., Hutchinson, J. R. & Blemker, S. S. Are mice good models for human neuromuscular disease? Comparing muscle excursions in walking between mice and humans. *Skelet. Muscle* **7**, 26 (2017).
56. Launikonis, B. S. & Ríos, E. Store-operated Ca^{2+} entry during intracellular Ca^{2+} release in mammalian skeletal muscle. *J. Physiol.* **583**, 81–97 (2007).
57. Duke, A. M., Hopkins, P. M., Calaghan, S. C., Halsall, J. P. & Steele, D. S. Store-operated Ca^{2+} Entry in Malignant Hyperthermia-susceptible Human Skeletal Muscle. *J. Biol. Chem.* **285**, 25645–25653 (2010).
58. Din, M. et al. Human brown adipose tissue [15O]O₂ PET imaging in the presence and absence of cold stimulus. *Eur. J. Nucl. Med. Mol. Imaging* **43**, 1878–1886 (2016).
59. Stephenson, D. G. & Williams, D. A. Calcium-activated force responses in fast- and slow-twitch skinned muscle fibres of the rat at different temperatures. *J. Physiol.* **317**, 281–302 (1981).
60. Stephenson, D. G. Modeling the mechanism of Ca^{2+} release in skeletal muscle by DHPs easing inhibition at RyR I1-sites. *J. Gen. Physiol.* **156**, e202213113 (2024).
61. Harrison, S. & Bers, D. The effect of temperature and ionic strength on the apparent Ca-affinity of EGTA and the analogous Ca-chelators BAPTA and dibromo-BAPTA. *Biochim. Biophys. Acta BBA - Gen. Subj.* **925**, 133–143 (1987).
62. Sherman, B. T. et al. DAVID: a web server for functional enrichment analysis and functional annotation of gene lists (2021 update). *Nucleic Acids Res* **50**, W216–W221 (2022).
63. Hsiao, J. J., Potter, O. G., Chu, T.-W. & Yin, H. Improved LC/MS Methods for the Analysis of Metal-Sensitive Analytes Using Medronic Acid as a Mobile Phase Additive. *Anal. Chem.* **90**, 9457–9464 (2018).
64. Adams, K. J. et al. Skyline for Small Molecules: A Unifying Software Package for Quantitative Metabolomics. *J. Proteome Res.* **19**, 1447–1458 (2020).

Acknowledgements

We thank Luke Pearce for performing some skinned fibre experiments; Sarah Reed and Aven Lee for performing the mass spectrometry work. We are also grateful to Sean Millard (University of Queensland, Brisbane) and Xaver Koenig (Medical University of Vienna) for helpful comments on the manuscript. This work was supported by research grants from The Jain Foundation and an Australian Research Council Discovery Project (DP220102018) to B.S.L.

Author contributions

Performed experiments: A.M.H., C.R.L., J.R.K., M.P.H.; designed experiments: A.M.H., C.R.L., J.R.K., M.P.H.; J.E.H. & B.S.L.; analyzed data: A.M.H., C.R.L., J.R.K., M.P.H.; J.E.H., & B.S.L.; wrote the paper: A.M.H., J.E.H., & B.S.L.

Competing interests

The authors declare no competing interests.

Additional information

Supplementary information The online version contains supplementary material available at <https://doi.org/10.1038/s41467-025-58393-2>.

Correspondence and requests for materials should be addressed to Bradley S. Launikonis.

Peer review information *Nature Communications* thanks Stephen Cannon, Muthu Periasamy, and the other, anonymous, reviewer(s) for their contribution to the peer review of this work. A peer review file is available.

Reprints and permissions information is available at <http://www.nature.com/reprints>

Publisher's note Springer Nature remains neutral with regard to jurisdictional claims in published maps and institutional affiliations.

Open Access This article is licensed under a Creative Commons Attribution-NonCommercial-NoDerivatives 4.0 International License, which permits any non-commercial use, sharing, distribution and reproduction in any medium or format, as long as you give appropriate credit to the original author(s) and the source, provide a link to the Creative Commons licence, and indicate if you modified the licensed material. You do not have permission under this licence to share adapted material derived from this article or parts of it. The images or other third party material in this article are included in the article's Creative Commons licence, unless indicated otherwise in a credit line to the material. If material is not included in the article's Creative Commons licence and your intended use is not permitted by statutory regulation or exceeds the permitted use, you will need to obtain permission directly from the copyright holder. To view a copy of this licence, visit <http://creativecommons.org/licenses/by-nc-nd/4.0/>.

© The Author(s) 2025